

Exploring Potential Mechanisms for the Initiation of Solifluction Patterns

Rachel C. Glade^{1,2*}, JohnPaul Sleiman¹, Alice Quillen³, David Cúñez¹, Sarah Williams¹

¹Department of Earth and Environmental Sciences, University of Rochester, Rochester 14580, USA.

²Department of Mechanical Engineering, University of Rochester, Rochester 14580, USA.

³Department of Physics, University of Rochester, Rochester 14580, USA.

*Corresponding author. Email: rachel.glade@rochester.edu

This is a non-peer reviewed preprint submitted to Earth Arxiv.

1 **Exploring Potential Mechanisms for the Initiation of**
2 **Solifluction Patterns**

3 **Rachel C. Glade^{1,2*}, JohnPaul Sleiman¹, Alice Quillen³, David Cúñez¹,**
4 **Sarah Williams¹**

5 ¹Department of Earth and Environmental Sciences, University of Rochester, Rochester 14580, USA

6 ²Department of Mechanical Engineering, University of Rochester, Rochester 14580, USA

7 ³Department of Physics, University of Rochester, Rochester 14580, USA

8 **Key Points:**

- 9
- 10 • Solifluction patterns are distinct from common fluid instabilities, though they bear a striking resemblance
 - 11 • Solifluction patterns likely form due to topographic bump-dependent effective viscosity, similar to non-inertial oobleck waves
 - 12 • We present a new conceptual model of the necessary and sufficient ingredients for the initiation and growth of solifluction patterns
- 13
- 14

Abstract

Hillslopes in arctic regions commonly display large-scale features—known as solifluction patterns—that form due to the exceedingly slow downhill movement of frost-heaved soil. Here we use a combination of remote sensing data, linear stability analysis, numerical modeling, and review of a wide range of literature to evaluate several working hypotheses for the necessary and sufficient conditions needed to form solifluction patterns. We find that despite striking visual similarity, fluid buckling, wrinkling, dripping, and roll wave patterns are not directly analogous to solifluction patterns. However, broadly inspired by non-inertial instabilities observed in shear-thickening oobleck (cornstarch mixed with water), we propose a conceptual framework for the formation of solifluction instabilities that relies on spatial heterogeneity of soil velocities in the presence of random frost heave-induced topographic bumps. More broadly, this study illustrates both caveats and the potential for success in drawing inspiration from diverse fields to understand pattern formation in the complex granular and fluid materials on Earth’s surface.

Plain Language Summary

Slowly flowing soil in some of the coldest places on Earth produces large scale features called solifluction patterns that strongly resemble a variety of different fluid patterns, like rainwater flowing down window glass or icing dripping down a cake. We found that despite their striking similarity, the physical ingredients needed to form solifluction patterns are distinct from those found in everyday fluids. Perhaps the closest analogous fluid pattern was only recently discovered—waves formed in oobleck (cornstarch mixed with water). This requires unique behavior in which the flow stiffens at the downhill side of bumps, causing a buildup of material behind it and the ultimate formation of waves. Our work, which includes mathematical theory and computer modeling, shows that solifluction patterns form in a similar way due to spatial differences in soil moisture at the front of bumps on the landscape. This demonstrates how patterns in everyday fluids can be compared and contrasted with complex patterns in sediment to better understand how Earth’s surface evolves.

1 Introduction

Periglacial hillslopes subjected to frequent freeze-thaw cycles commonly host distinctive spatial soil patterns including sorted circles and stripes (Kessler & Werner, 2003), frost wedge polygons (Lachenbruch, 1962), and solifluction terraces and lobes (Matsuoka, 2001; R. C. Glade et al., 2021), which we focus on in this paper (Fig. 1A,B). Originally coined by Andersson (1906) to mean the downslope motion of saturated soil in any environment, the term “solifluction” is now generally used to describe downslope periglacial soil motions that occur due to a combination of four processes: 1) needle ice creep, which occurs only at the thin surface layer (Li et al., 2021), 2) frost creep, in which soil is lofted normal to the slope in the winter as ice lenses form within the soil (Rempel, 2007; Pepin & Style, 2013), then settles vertically in the spring as the soil thaws, resulting in a net downslope motion (R. S. Anderson & Anderson, 2010; Rempel, 2007) 3) gelifluction, or bulk downslope deformation of partially-to-fully saturated soil for a brief period of time during spring thaw (Benedict, 1976; Harris & Davies, 2000), and 4) plug-like flow (Matsuoka, 2001). Together these processes lead to slow downslope on order of mms to cms per year (French, 2017). In this study we focus on mechanisms 2 and 3 as the most relevant for solifluction pattern formation (though future work may explore the role of 1 and 4). A ubiquitous erosional process in cold regions on Earth and potentially on Mars (Gastineau et al., 2020; Johnsson et al., 2012; Sleiman et al., 2024), solifluction is especially relevant as the need to predict and mitigate slope stability due to thawing permafrost becomes increasingly urgent (Rowland et al., 2010). Further, a better understanding of these patterns may enable the use of solifluction feature as indicators of paleoclimate on

65 Earth (e.g., (Merritts & Rahnis, 2022)) or Mars (Johnsson et al., 2012; Sleiman et al.,
66 2024).

67 While much work has been done to characterize these features in the field (Harkema
68 et al., 2023; Draebing & Eichel, 2017; Matsuoka, 2001; French, 2017; Matsuoka, 2001)
69 and in the lab (Harris, 1996; Harris et al., 2003, 2008; Harris, 1993), our understanding
70 of the physical underpinnings of solifluction and the resulting patterns remains limited.
71 This stems from the complexity of the deformation style of icy soils—which exhibit sea-
72 sonally variable strong heterogeneity in grain size, water and ice content (R. C. Glade
73 et al., 2021) and can behave both as a fluid and solid under different conditions (Jerolmack
74 & Daniels, 2019)—as well as the difficulty in obtaining accurate and sufficient measure-
75 ments for very slow-moving soils that exist in logistically challenging field locations.

76 Solifluction patterns may be broken into two distinct parts: terraces, which are wave-
77 like patterns oriented downslope (Fig. 1A), and lobes, which are finger-like patterns that
78 form cross-slope, often (but not always) at terrace fronts (Fig. 1B). A recent study ar-
79 gued that cross-slope solifluction lobe wavelengths (i.e., solifluction tread width) may be
80 analogous to finger-like instabilities found at the front of surface-tension dominated fluid
81 flows known as “contact line instabilities,” such as paint dripping down a wall or oil fin-
82 gering in a frying pan (R. C. Glade et al., 2021). In this framework, (R. C. Glade et al.,
83 2021) proposed that competition between gravity and enhanced soil cohesion (or another
84 mechanism of stalling) results in the formation of lobes, analogous to competition be-
85 tween the driving force and surface tension in thin film flows (Huppert, 1982). The au-
86 thors showed that a scaling analysis based on fluid-like motions of soil could capture the
87 first order characteristics of solifluction lobe wavelength and morphology using a large
88 dataset from Norway (R. C. Glade et al., 2021). Another recent study found similar scal-
89 ing in lobate patterns on Mars, suggesting similar formational mechanisms (Sleiman et
90 al., 2024). These first-order scaling analyses have the advantage of being largely insen-
91 sitive to rheology (the deformation style, or relationship between shear stress and strain
92 rate); however, they cannot predict the onset of the instability or provide a detailed phys-
93 ical model of soil motion. Further, these studies did not identify a particular mechanism
94 of stalling at lobe fronts, and did not attempt to explain the primary instability of ter-
95 race formation.

96 Inspired by this and recent studies in non-Newtonian fluids, here we use a combi-
97 nation of scaling analysis, linear stability analysis, remote sensing and a broad review
98 of literature from different fields to explore different possible mechanisms for the forma-
99 tion of solifluction terraces and their downslope wavelengths (defined as the downslope
100 distance between terrace fronts or “risers”). Perhaps most importantly, our work demon-
101 strates which simple models (frost heave + fluid-like flow) and potentially analogous sys-
102 tems (buckling instabilities, roll waves) are *not* able to explain the formation of solifluc-
103 tion terraces, while using recent findings in soft matter physics—oobleck waves, or pat-
104 terns developed in shear thickening suspensions of cornstarch mixed with water—to de-
105 velop a new qualitative conceptual model for solifluction patterns, highlighting possible
106 mechanisms for the onset of non-inertial instabilities and suggesting future field and ex-
107 perimental work. Our proposed model may explain both terraces and lobes, as both in-
108 stabilities likely require similar behavior focused at soil fronts. We also discuss poten-
109 tial reasons why these patterns are only found in cold landscapes, despite the fact that
110 soil creeps downhill due to gravity and disturbance in every climate zone (Deshpande
111 et al., 2021; Pawlik & Šamonil, 2018). Our study can be viewed as a thought paper that
112 synthesizes a number of competing hypotheses for solifluction pattern formation, point-
113 ing the way forward for future field, experimental, and theoretical work on this rich prob-
114 lem.

115 Section 2 discusses what we know about solifluction processes, including field and
116 lab measurements of solifluction motions that ground our theoretical discussion in real
117 data. Section 3 examines the possibility that solifluction terraces are an example of a

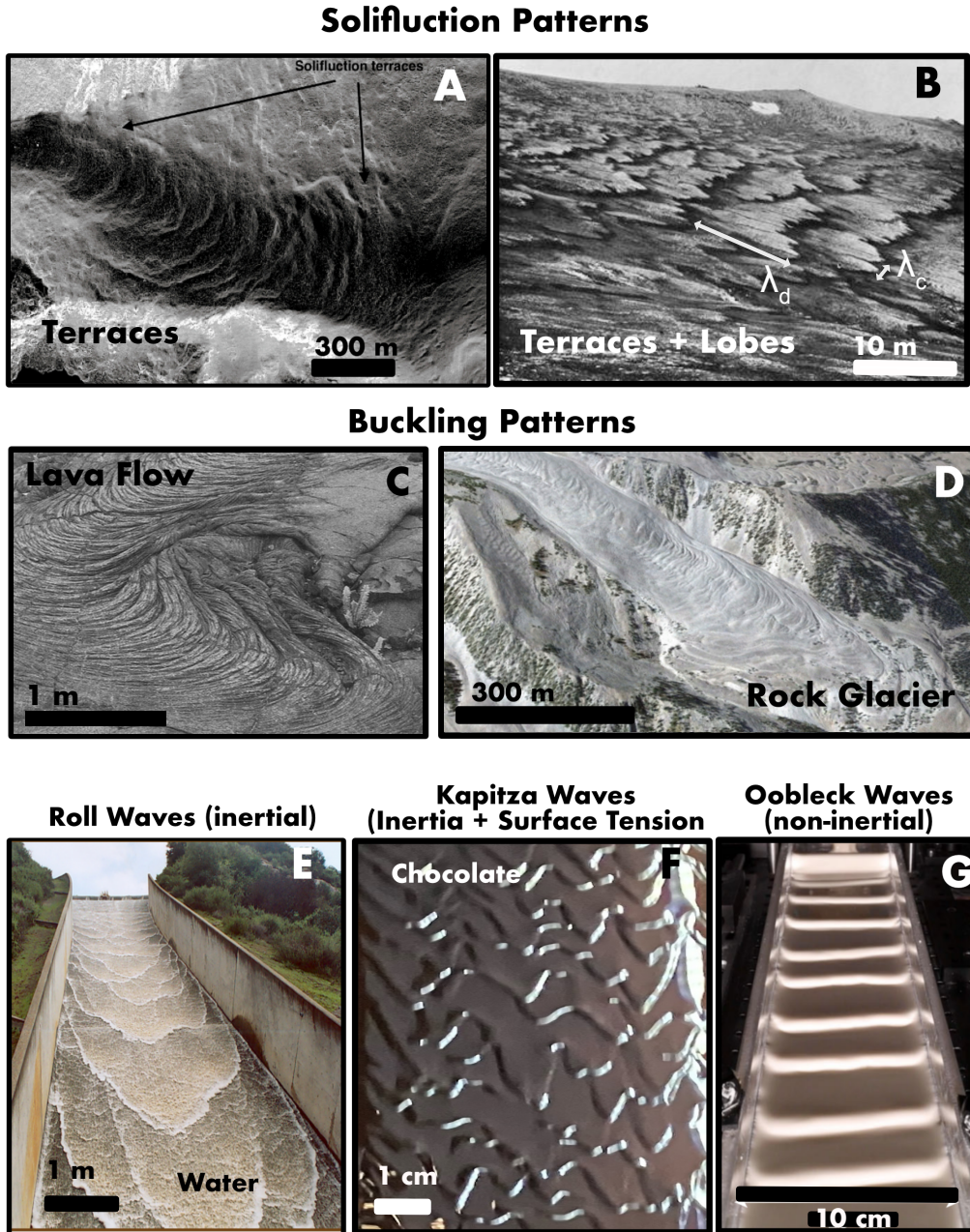


Figure 1. Photos of solifluction terraces and possible analogues explored in this paper. (A) LiDAR-derived slope map of solifluction terraces at Niwot Ridge, Colorado. (B) Solifluction patterns in Chicken Creek, AK with downslope wavelength λ_d and cross-slope wavelength λ_c illustrated. Photo by Philip S. Smith. (C) Buckling of a lava flow, from (Slim et al., 2009). Photo by Dr. Ron Schott. (D) Buckling on a rock glacier at Mt. Sopris, Colorado. From Google Earth. (E) Inertial roll waves at Turner reservoir, CA. Photo by Victor Ponce. (F) Kapitza waves in a chocolate waterfall. Photo by Chloe Lindeman. (G) Non-inertial experimental oobleck waves, from (Darbois Texier et al., 2020).

118 buckling instability. Section 4 uses a simple fluid scaling analysis to explore downslope
 119 wavelength scaling with soil thickness and slope in remote sensing data from Norway.
 120 Section 5 introduces the concept of linear stability analysis by evaluating the stability
 121 of our simple fluid formulation. Section 6 evaluates the stability of a more complex for-
 122 mulation that reproduces the vertical velocity profiles observed in the field. Section 7
 123 evaluates the stability of a formulation inspired by oobleck waves, in which viscosity in-
 124 creases at the front of bumps. Section 8 presents our conceptual model inspired by our
 125 analysis, highlighting the necessary and sufficient ingredients to produce solifluction pat-
 126 terns.

127 2 Solifluction Processes

128 While solifluction processes and rates have been documented in the field for over
 129 a century (R. S. Anderson & Anderson, 2010), due to the complexity of the temporally
 130 evolving soil/ice/water mixture, a straightforward description of the rheology of solifluct-
 131 ing soil remains out of reach. During fall freeze up, ice lenses form in the soil as super-
 132 cooled water migrates along grain boundaries and self organizes into discrete lenses of
 133 ice (Taber, 1930; Rempel, 2007; Peppin & Style, 2013) (while this fascinating and com-
 134 plex phenomenon deserves further consideration, a complete review of the relevant lit-
 135 erature is outside the scope of this study). This leads to frost heave, which lofts soil up-
 136 wards during fall freeze-up. One common misconception is that frost heave occurs only
 137 due to the volumetric expansion of water as it turns to ice; however, in the presence of
 138 ice lenses water migrates from the pore space to discrete lenses, resulting in frost heave
 139 of up to tens of centimeters at the surface—typically far surpassing simple expansion due
 140 to the volume change of water to ice, which can only cause a 9% change in volume of
 141 the soil column (Rempel, 2007). Ice lens formation also depends on the presence of per-
 142 mafrost and whether freezing is top-down or two-sided (Harris et al., 2008). During the
 143 winter, presumably little to no motion occurs in the soil (though direct observation of
 144 soil motions are challenging under the snowpack). In the summer, thaw begins from the
 145 top down, causing 1) frost creep due to thaw consolidation vertically downward and 2)
 146 saturation and subsequent deformation of the soil (R. S. Anderson & Anderson, 2010),
 147 known as “gelifluction” (Fig 2B) and 3) sometimes, retrograde motion uphill, thought
 148 to be due to cohesive effects (Matsuoka, 2001). Frost creep can be conceptualized as the
 149 lofting of soil along a direction normal to the slope, driven by ice lens formation during
 150 freeze events, followed by vertical settling upon thaw (Fig. 2B). With this conceptual
 151 model in mind, (R. S. Anderson & Anderson, 2010) use a simple geometric frost heave
 152 and settling model to define event-scale frost creep flux as:

$$q_i = -\frac{\rho_b \beta}{2} \frac{d\zeta}{dx} d_f^2 \quad (1)$$

153 where ρ_b is the bulk density of the soil, β is the soil strain upon freezing, $d\zeta/dx$ is
 154 the surface slope, and d_f is the penetration depth of a particular frost event. They point
 155 out that this is akin to a diffusive flux commonly used for hillslope sediment transport
 156 , albeit one that acknowledges the processes that contribute to the diffusivity. Note that
 157 we use the convention of positive flux downhill in the positive x direction, leading to the
 158 negative sign in Eqn. 1. The event scale flux can be extended to an annual mean flux.
 159 While this example of a classic diffusive flux may be useful for larger timescales of land-
 160 scape evolution, it is clear that due to the incredible stability and smoothing behavior
 161 of diffusion processes, it is unlikely that they will be able to produce solifluction insta-
 162 bilities. Further, the morphology of solifluction lobes and terraces points toward a more
 163 complex story in which soil can maintain very steep—even past vertical—fronts (Benedict,
 164 1970), precluding a simple diffusive-like process (Fig 2A). Solifluction consists of not only
 165 frost creep , but also gelifluction, or the bulk deformation of soil upon spring thaw (Harris

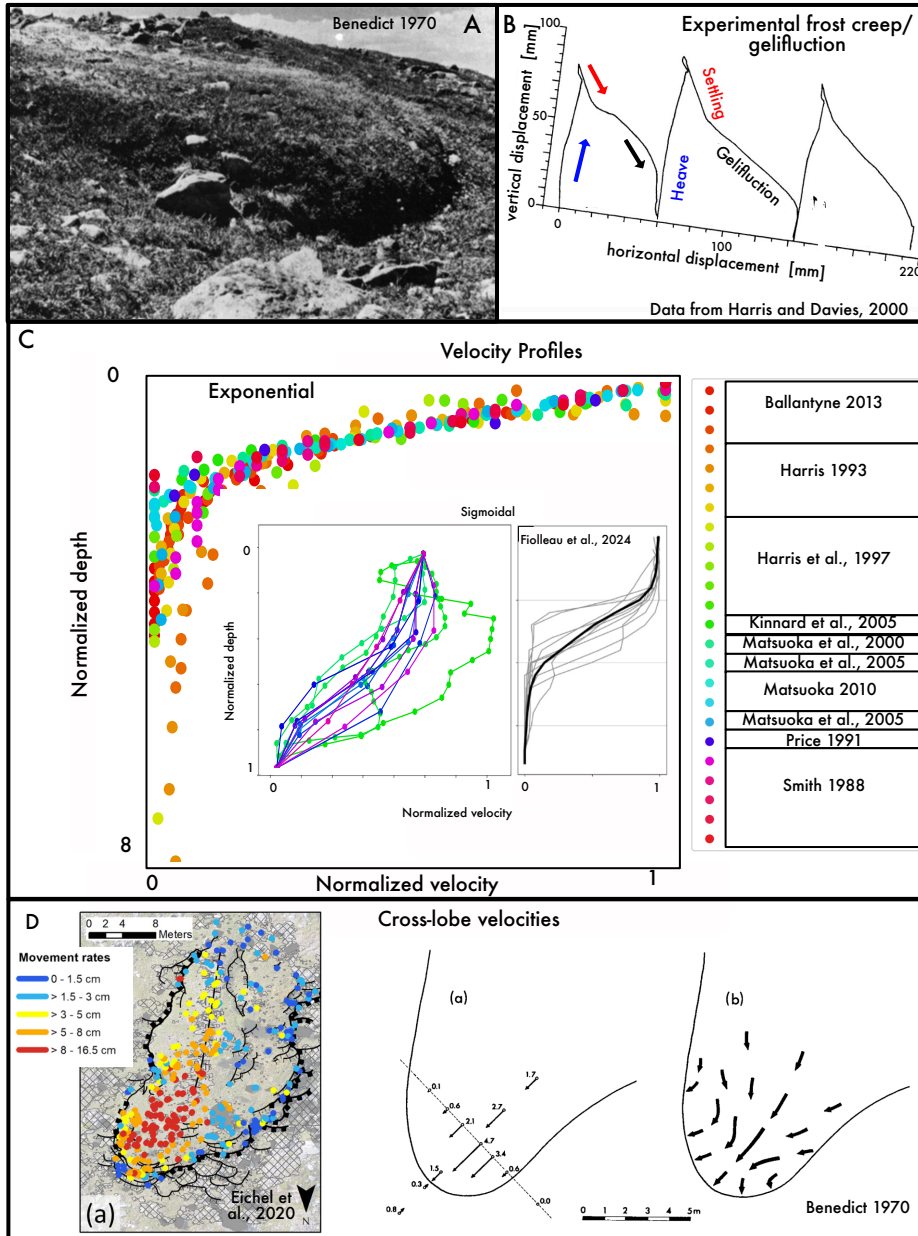


Figure 2. Field data illustrating soliflucting soil motions. (A) Photo of a solifluction lobe from Niwot Ridge, CO illustrating steep, overhanging front (photo from (Benedict, 1970)) Copyright Taylor & Francis. (B) Experimental solifluction displacements illustrating frost heave, settling, and gelifluction using data from (Harris & Davies, 2000). (C) Time-averaged velocity profiles compiled from the literature show highest velocity at the surface. While most profiles are exponential with depth, faster soil velocities result in a sigmoidal profile (insets). (D) Field measurements of differences in soil velocity across solifluction lobes. Left: drone photogrammetry-derived soil movement rates (cm/yr) from (Eichel et al., 2020)). Right: Soil velocity measurements in cm/yr from (Benedict, 1970)). Copyright INSTAAR.

3 The Allure of Visual Similarity: Buckling Instabilities and Roll Waves

Here we explore possible connections between solifluction terrace patterns and two visually similar fluid patterns. At first glance, solifluction terraces bear a striking resemblance to buckling instabilities (Fig. 1). This led us down an immense rabbit hole of literature spanning multiple disciplines. Soft materials, including thin elastic sheets and thin film fluids, commonly undergo buckling instabilities in which the material self-organizes to compress and form folds or buckles (Fig. 1C,D). Buckling has been shown to occur at a variety of length and time scales in both geological processes and everyday materials due to 1) compression (e.g., ice sheets (Coffey et al., 2022), rock folds (Biot, 1961), buckling of subducted lithospheric plates (Ribe et al., 2007), buckling of elastic plates (N. J. Balmforth et al., 2008), coiling of honey (Ribe, 2004) and/or 2) strain mismatch between different layers of fluid or soft materials, particularly where a resistant layer overlies a more deformable layer (e.g., transverse ridges in rock glaciers (Loewenherz et al., 1989), lava flows (Griffiths, 2000), an elastic sheet overlying a shear fluid (Slim et al., 2012), growth-induced instabilities in multilayer materials, like pumpkins or shar pei dogs (Wang & Zhao, 2015)) (see (Slim et al., 2012) for a nice brief review of the literature).

Compression buckles can occur all at once in a material compressed from both sides (e.g., (Biot, 1961)) or will occur in succession for a material undergoing compression from one side (e.g., (Ribe, 2003; Ribe et al., 2007; Skorobogatiy & Mahadevan, 2000; Blake & Bejan, 1984), as can be observed when pouring cake batter into a pan. While the mechanism is similar in all cases of compression buckling, the governing equations and therefore stability criteria and wavelength predictions are unique to the specific geometry and materials for each case. (Biot, 1961) first studied folding in viscoelastic rock layers embedded within rocks of different effective viscosities when compressed from both sides, finding that wavelengths tend to be on order of 20-50 times the thickness of the layer, depending on the viscosity contrast. (Treagus, 1973) found that rock layers oblique to the axis of principal compression behave similarly. Periodic folding of a vertically falling viscous sheet (Ribe, 2003) exhibits wavelengths primarily dependent on the fall velocity and sheet thickness, with relevance not only for pouring fluids like honey, but also for subducting plates (Ribe et al., 2007). (Coffey et al., 2022) found that buckling of ice sheets depends only on the compressional pressure in the ice, not on ice thickness.

In a large dataset of solifluction terraces in Norway, wavelength to soil thickness ratios range from 10-70 (R. C. Glade et al., 2021) (Fig. 3), not dissimilar from ratios found in folding under compression (Biot, 1961). While hillslopes are unlikely to be compressed on both top and bottom, it is plausible that soil creeping down a concave up slope may experience compression at the base of the slope. If this were the case, we might expect that most solifluction terraces form on concave-up slopes where compression may occur at the base. However, profiles of terraced slopes across Norway demonstrate that solifluction terraces can form on slopes of any curvature (Fig. 3). It is possible that some of these are paleoterraces developed at a time when hillslope curvature was different. However, the morphology of solifluction terraces is also strikingly different from that of compression buckles; wavelengths are quite large, on order of tens of meters, and terraces gently grade into a steep front, rather than demonstrating symmetrical periodic folds typical of the settings mentioned above. While the compression buckling mechanism is unlikely, a good field test could be done in which terraces are radiometrically dated (e.g., (Kinnard & Lewkowicz, 2006)). If compression buckling were indeed the mechanism for the instability, we would expect to see progressively younger terraces moving from the bottom to the top of the slope. Note that we do see smaller scale “rumples” or buckles at the toe of active layer detachments and earthflows that are good candidates for compression buckling (Del Vecchio et al., 2022).

The second common buckling mechanism involving strain mismatch between different layers, particularly with a viscous fluid or elastic sheet riding atop a less viscous fluid, could be relevant for soliflucting soil. This situation results in folds that strongly

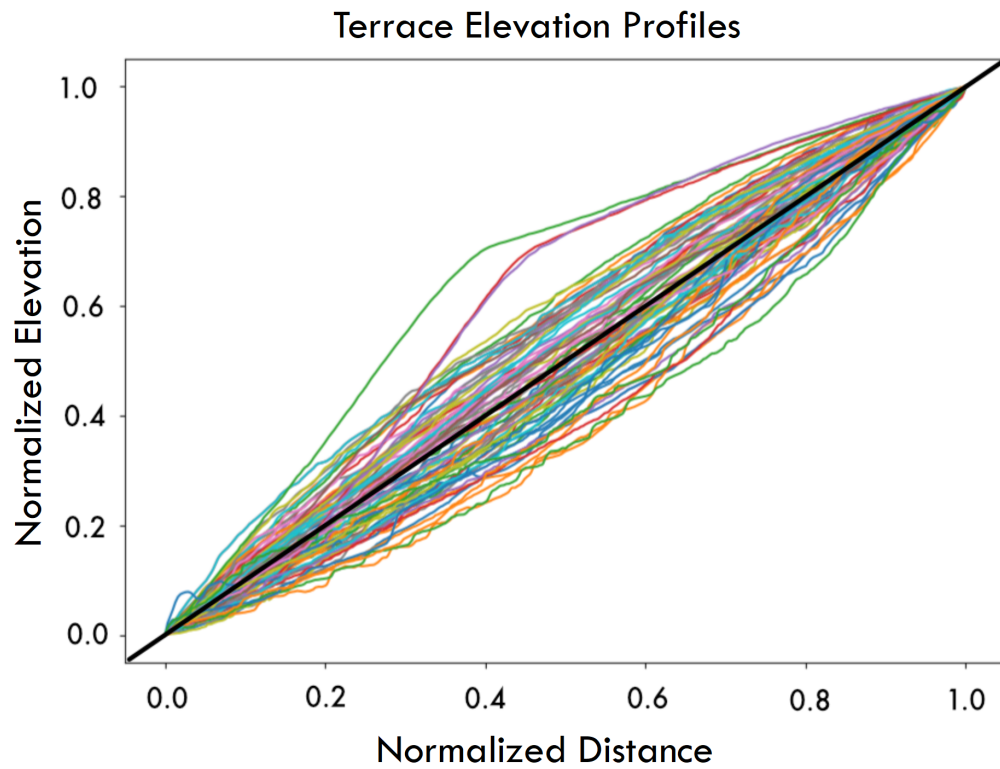


Figure 3. Downslope elevation profiles of sites with solifluction terraces, normalized by max and min elevation and distance for each downslope profile drawn from the bottom to the top of a series of terraces. Note the wide variety of profiles curvatures- many terraces occur on convex-up slopes, bringing into question the argument that terraces form due to compressional buckling. Different colors only help the eye to differentiate individual profiles.

resemble solifluction terraces (Fig. 1C,D). Does soliflucting soil contain multiple layers that could allow for this mechanism to occur? At first glance, it seems that the surface layer of vegetation could induce buckling, much like the crust at the surface of a lava flow produces folds (Fink, 1980), or the debris on top of a rock glacier produces ridges (Loewenherz et al., 1989) at large wavelengths (tens of meters) that are comparable to solifluction terrace wavelengths. These studies find that buckling wavelength is primarily a function of the thickness and rigidity of the surface layer, with a wavelength roughly an order of magnitude larger than the thickness of that layer (Loewenherz et al., 1989). However, typical tundra vegetation layers are only tens of centimeters thick—while that could potentially result in smaller wavelengths ~ 5 m, it could not explain wavelengths on order of many tens or hundreds of meters (Fig. 1A; Fig. 4). It is possible that soil moisture, ice conditions, or accumulation of coarse grains (e.g., stone-banked lobes (Matsuoka, 2001)) lead to a thicker drier “skin” at the surface of the soil with higher effective viscosity. However, vertical displacement profiles of soliflucting soil show little to no decrease in velocity at the surface; in fact, there is a marked increase in velocity at the surface (Fig. 2C), presenting a strong argument against a multilayer buckling mechanism.

Another strikingly similar instability (Fig. 1E, F) occurs when a thin layer of fluid flowing down a plane produces self-organized patterns known as roll waves or Kapitza waves (Kapitza, 1949) (notably, this seminal study was conducted by father and son team while on political house arrest in Soviet Russia (Chang et al., 1994)). Roll waves can be seen in rainwater flowing down a street, or in the sheets of water cascading down a waterfall. They can also be observed in granular suspensions such as mudflows (N. Balmforth & Liu, 2004). These instabilities occur when infinitesimal perturbations in flow thickness become unstable and grow as thicker flow moves faster. Roll waves probably most closely resemble the morphology of solifluction waves, with the ability to form both down-slope and cross-slope waves that override each other and coalesce (Fig. 1F). However, there is a key requirement for the initiation of roll waves that is conspicuously missing in solifluction: inertia. In Newtonian flows, a critical finite Reynolds Number $Re = \rho UL/\mu$ —typically on order of 10 or greater—is required for onset of roll waves (M. K. Smith, 1990). While less is known about roll waves in non-Newtonian flows, they have also been shown to exhibit a critical Re greater than 1 (N. Balmforth & Liu, 2004; Depoilly et al., 2024). Assuming an effective viscosity of 10^5 – 10^{12} Pa-s (R. C. Glade et al., 2021), with velocities on order of 1cm/yr and a length scale of a meter, Reynolds numbers in soliflucting soil could be as low as 10^{-22} : unquestionably non-inertial. We can also evaluate the inertia of our system a different way with the inertial number $I = \dot{\gamma}d/\sqrt{P/\rho_p}$ from granular physics (Guazzelli & Pouliquen, 2018), where $\dot{\gamma}$ is the shear rate, d is the particle diameter, P is the pressure due to grain contacts and ρ is the density of the particles. Using a characteristic shear rate of 10^{-9} /s from vertical displacement profiles observed in the field (Figure 2C; (R. Glade, 2026)), a characteristic particle size of .01 mm (silt), a pressure $P = \rho_b g H \approx (1500 \text{ kg/m}^3)(9.8 \text{ m/s}^2)(1 \text{ m}) \approx 15000 \text{ Pa}$, and particle density of 2650 kg/m^3 , we estimate $I \approx 10^{-18}$. This is many orders of magnitude below the threshold $I \approx 10^{-3}$ for quasistatic (i.e., non-inertial) flow, as expected for slowly creeping soils (Jerolmack & Daniels, 2019). Thus, mechanisms for the onset of solifluction instabilities must not rely on the presence of inertia. We formally show the unconditional stability of a simple non-inertial fluid flow in section 5.1. We conclude that solifluction terraces sadly cannot be explained by alluringly simple direct analogies to fluid buckling or roll wave instabilities.

4 Scaling Analysis for Solifluction Terraces

We now seek an explanation for solifluction terraces that does not rely on the presence of multiple layers, compression, or inertia. Here we develop a series of simple theoretical formulations to explore other possible mechanisms for the onset of solifluction instabilities. Given 1) the similarities between solifluction patterns and fluid instabili-

320 ties (R. C. Glade et al., 2021), 2) the complexity and uncertainty of solifluction rheol-
 321 ogy, and 3) the general fluid-like behavior of soft matter including earth materials (Jerolmack
 322 & Daniels, 2019), for simplicity we ground our formulations in the language of fluid me-
 323 chanics; however, we emphasize that future work could (and should) explore similar for-
 324 mulations in the realm of granular physics, soil mechanics, and even statistical physics
 325 that acknowledges the stochastic and possibly non-continuum nature of seasonal soil mo-
 326 tions (Furbish et al., 2021).

327 In this section we present a scaling analysis for a simple fluid flowing down an in-
 328 clined plane in an effort to predict the wavelength scaling for solifluction terraces. In the
 329 case of solifluction, the “fluid” is mobile soil and the inclined plane is either bedrock or
 330 an immobile permafrost layer. Note that this approach follows directly from that of (R. C. Glade
 331 et al., 2021) for the cross-slope patterns of solifluction lobes, but ignores any dynamics
 332 in the cross-slope direction to focus on dynamics in the downslope (x) direction. Because
 333 the rheology of soliflucting soil is unknown, we begin with a simple fluid rheology that
 334 includes the role of hydrostatic pressure, and see that similar to findings in (R. C. Glade
 335 et al., 2021) for cross-slope patterns, the resulting first-order scaling, though noisy, gen-
 336 erally agrees with measurements of downslope solifluction terrace wavelengths from re-
 337 mote sensing imagery in Norway. While this alone does *not* prove that soliflucting soil
 338 behaves as a simple fluid, it importantly offers *support* for a first-order fluid-like behav-
 339 ior that cannot be disproved by our data. Any fluid-like material (even with complex
 340 non-Newtonian rheology) should obey scaling similar to what we find here.

341 We then present a linear stability analysis, illustrating that our simple choice of
 342 non-inertial governing equation with Newtonian rheology is unconditionally stable and
 343 therefore not sufficient to explain the onset of the solifluction terrace instability. How-
 344 ever, to be clear, this does not invalidate the utility of the scaling analysis, which sim-
 345 ply predicts scaling and not a preferred wavelength or conditions for the instability. In
 346 subsequent sections we explore more complex formulations of the problem.

347 4.1 1D scaling analysis for a simple fluid

348 This and all the following analyses begin with the setup of fluid flow with verti-
 349 cal thickness H on an inclined plane. Assuming a simple non-inertial fluid-like rheology
 350 for soil transport, we define the basal shear stress as (R. S. Anderson & Anderson, 2010):

$$\tau_{0x} = \rho g H S - \rho g H \frac{\partial H}{\partial x} \quad (2)$$

351 where ρ is the bulk density of soil, g is gravitational acceleration, H is the soil thick-
 352 ness, S is the topographic slope $\sin \theta$, and x is the horizontal component (defined as in-
 353 creasing downhill). The first term on the right hand side is the shear stress due to the
 354 overlying weight of the soil on an inclined plane, while the second term is the hydrostatic
 355 pressure resulting from bumps in the topography (e.g., resulting from differential frost
 356 heave, see Section 8). Because we do not know the precise rheology of soliflucting soil,
 357 we define a bulk dynamic viscosity μ such that:

$$\tau_{0x} = \mu \frac{U}{H} \quad (3)$$

358 where U is the vertically-averaged velocity in the downslope (x) direction. Setting 2 equal
 359 to 3 we find:

$$U(x) = \frac{\rho g H^2}{\mu} \left(S - \frac{\partial H}{\partial x} \right) \quad (4)$$

360 According to continuity:

$$\frac{\partial H}{\partial t} + \frac{\partial q_x}{\partial x} = 0 \quad (5)$$

361 where t is time and $q_x = HU$ is the flux. Evaluating $\frac{\partial q_x}{\partial x}$ and plugging into 5, we find:

$$\frac{\partial H}{\partial t} + \frac{\rho g}{\mu} \left[3H^2 S \frac{\partial H}{\partial x} - 3H^2 \left(\frac{\partial H}{\partial x} \right)^2 - H^3 \frac{\partial^2 H}{\partial x^2} \right] = 0 \quad (6)$$

362 Assuming the local term is negligible near a flow front and terms that contain products
363 of derivatives are small compared to the other terms, we find:

$$0 = 3S \frac{\partial H}{\partial x} - H \frac{\partial^2 H}{\partial x^2} \quad (7)$$

364 Now we non-dimensionalize terms such that:

$$\begin{aligned} x &= \hat{\lambda} \lambda, \\ H &= \hat{H} H_0 \end{aligned} \quad (8)$$

365 where H_0 is a characteristic soil thickness and λ is a characteristic length in the x di-
366 rection. Substituting these into 7 yields:

$$3S \frac{H_0}{\lambda} \frac{\partial \hat{H}}{\partial \hat{\lambda}} - \frac{H_0^2 \hat{H}}{\lambda^2} \frac{\partial^2 \hat{H}}{\partial \hat{\lambda}^2} = 0 \quad (9)$$

367 Simplifying and retaining only the dimensional coefficients, we find:

$$\lambda_d \sim \frac{H_0}{3S} \quad (10)$$

368 (we rewrite λ as λ_d here, under the assumption that λ relates to the downslope wave-
369 length of solifluction terraces (Figure 1B)). Eq. 10 suggests that terrace wavelength should
370 scale linearly with soil thickness divided by topographic slope, where thicker soil or shal-
371 lower slopes result in larger downslope wavelengths. The factor of 3 in the denomina-
372 tor may not be meaningful, as a full solution would likely include an additional constant.
373 Scaling is a first order analysis that is largely insensitive to the complexities of rheology.
374 To be clear, the scaling seen in 10 can be viewed as a minimum requirement for a sys-
375 tem to be considered fluid-like; however, agreement with that scaling does not “prove”
376 in any way that we have the proper governing equations for our system.

377 4.2 Solifluction Terrace Scaling from Remote Sensing Data

378 To determine whether this simple scaling agrees with observations, we use a high
379 resolution dataset from Norway (R. C. Glade et al., 2021) to measure downslope solifluc-
380 tion terrace wavelength γ , height h , and topographic slope S . Note that measured ter-
381 race height h is different from the initial height h_0 at the onset of the instability, adding
382 a source of error. While limited data prevent us from confidently determining the scal-
383 ing relationship, results show that terrace wavelength increases and may generally scale
384 linearly with h/S , with a large amount of scatter characteristic of remotely sensed data

385 of subtle topographic features. Each data point in Fig. 4 represents an average of wave-
 386 length, height and slope values from a single transect including multiple terraces taken
 387 from ~ 30 different sites across Norway (see (R. C. Glade et al., 2021) Methods). Ver-
 388 tical and horizontal lines represent standard error. Similar to (R. C. Glade et al., 2021),
 389 because scaling is typically not sensitive to details of rheology, this scaling suggests that
 390 solifluction patterns may generally obey fluid-like behavior. More cautiously, this scal-
 391 ing shows that solifluction patterns don't *not* obey fluid-like behavior. As discussed in
 392 the following sections, a better understanding of the rheology and other phenomenolog-
 393 ical aspects on the system are needed to predict the onset of the instability.

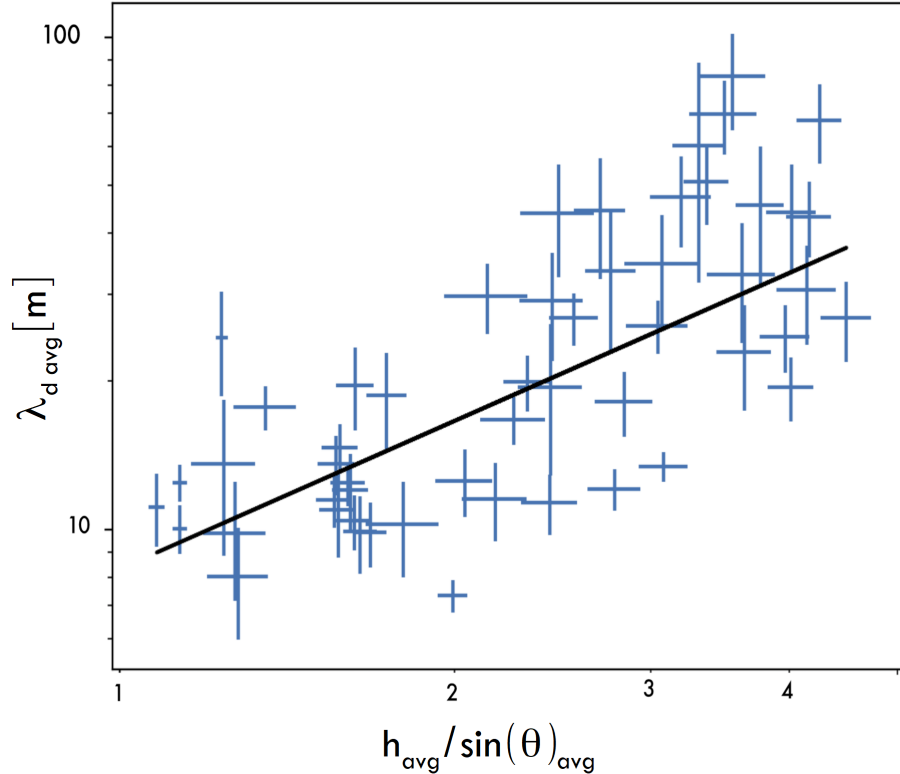


Figure 4. Scaling between downslope terrace wavelength, height and slope for from a large dataset in Norway (R. C. Glade et al., 2021). Each point represents the mean wavelength, height and slope from a given downslope-oriented transect. Vertical and horizontal lines represent standard error. Black line is the theoretical curve from our scaling analysis.

394 5 Evaluating Stability of Potential Solifluction Formulations

395 Here we turn to a series of linear stability analyses to determine the stability of dif-
 396 ferent fluid-like formulations to infinitesimal perturbations. First, we show that a sta-
 397 bility analysis for our simple fluid formulation (Eqn. 4) is unconditionally stable, and
 398 thus likely unable to explain the onset of the instability. In the following sections we build
 399 complexity to determine what general type of formulation may ultimately be able to ex-
 400 plain solifluction patterns. We also emphasize that a key aim of this study is to clearly
 401 explain why linear stability analysis is useful and to demonstrate how to conduct one
 402 for readers who may not be familiar with the technique.

5.1 Linear Stability Analysis for a Simple Fluid

Here we use linear stability analysis to formally demonstrate the stability of the above formulation for non-inertial flow, thus showing that solifluction terraces cannot be produced from the same instability as roll waves. We fully outline each step of the stability analysis in an effort to be accessible to readers who are not familiar with this technique. Subsequent stability analyses in this paper will be presented in shorter form with detailed analysis in Supplementary Materials. Essentially, a linear stability analysis explores the initial stability of an equation or set of equations when subjected to an infinitesimal perturbation around a base state. It is important to note that more complex nonlinear stability analyses (not attempted in this study) or numerical solutions are required to predict more complex behavior after the onset of the instability, nonlinear effects, or instabilities that require a finite amplitude initial perturbation (see example in Section 7.1).

Beginning with Eqn. 6 and ignoring the second term on the RHS that contains products of derivatives because they don't contribute first order terms, we have:

$$\frac{\partial H}{\partial t} + \frac{\rho g}{\mu} \left[3H^2 S \frac{\partial H}{\partial x} - H^3 \frac{\partial^2 H}{\partial x^2} \right] = 0 \quad (11)$$

Now we allow for a small perturbation to the soil depth H :

$$H(x, t) = H_0 + H_1(x, t) \quad (12)$$

where H_0 is the base state with uniform flow thickness, and H_1 is a first-order perturbation around this base state. Substituting Eqn. 12 into Eqn. 11, we have:

$$\frac{\partial(H_0 + H_1)}{\partial t} + \frac{\rho g}{\mu} \left[3(H_0 + H_1)^2 S \frac{\partial(H_0 + H_1)}{\partial x} - H^3 \frac{\partial^2(H_0 + H_1)}{\partial x^2} \right] = 0 \quad (13)$$

Note that H_0 is constant and therefore does not change with time or space, so can be removed from the derivatives. Expanding the parenthetical terms, this leaves us with:

$$\frac{\partial H_1}{\partial t} + \frac{3\rho g S}{\mu} (H_0^2 + 2H_0 H_1 + H_1^2) \frac{\partial H_1}{\partial x} - \frac{\rho g}{\mu} (H_0^3 + 3H_0^2 H_1 + 3H_0 H_1^2 + H_1^3) \frac{\partial^2 H_1}{\partial x^2} = 0 \quad (14)$$

Retaining only the terms that are linear in H_1 leaves with us the linearized governing equation:

$$\frac{\partial H_1}{\partial t} + \left(\frac{3\rho g S H_0^2}{\mu} \right) \frac{\partial H_1}{\partial x} - \left(\frac{\rho g H_0^3}{\mu} \right) \frac{\partial^2 H_1}{\partial x^2} = 0 \quad (15)$$

Now to do the stability analysis we assume a solution (Chandrasekhar, 2013) of the form:

$$H_1(x, t) = A_0 e^{\gamma t + i k x} \quad (16)$$

where A_0 is the initial amplitude, $k = 2\pi/\lambda$ is the wavenumber (where λ is the wavelength), and γ is a complex number where the real part represents the growth rate and the imaginary part represents the celerity of the waveform. For reference, the relevant derivatives are:

$$\frac{\partial H_1}{\partial x} = A_0 i k e^{\gamma t + i k x} \quad (17)$$

$$\frac{\partial^2 H_1}{\partial x^2} = -A_0 k^2 e^{\gamma t + i k x} \quad (18)$$

$$\frac{\partial H_1}{\partial t} = A_0 \gamma e^{\gamma t + i k x} \quad (19)$$

431 Substituting these into Eqn. 15 and simplifying, then solving for γ , we find:

$$\gamma = -\frac{\rho g H_0^3}{\mu} k^2 - i \frac{3 \rho g S H_0^2}{\mu} k \quad (20)$$

432 The sign of the real part of the growth rate σ determines the stability of the sys-
 433 tem; positive growth rate indicates instability, while negative growth rate indicates sta-
 434 bility. In our case, the real part of the growth rate is negative for all values of k , which
 435 means that the equation is unconditionally stable. The waveform decays to its base state
 436 with a rate that increases nonlinearly with k . The imaginary term is linear in k , show-
 437 ing that wave speed is constant for all k . In a more interesting result, we might find con-
 438 ditional stability such that the system becomes unstable for only certain values of k . In
 439 that case, stability analysis can often be used to determine the wavenumber associated
 440 with the maximum growth rate, which gives a prediction of the preferred wavelength of
 441 the instability (Whitehead, 1988). Our finding of unconditional stability for our simple
 442 fluid formulation most likely means that our chosen governing equations are not suffi-
 443 cient to explain the observed instability. Additionally, linear stability analysis only ex-
 444 amines stability in the face of an infinitesimal perturbation; some systems may require
 445 a finite amplitude A_0 in order to become unstable. It is possible that the real instabil-
 446 ity is nonlinear, thus requiring a trickier nonlinear stability analysis (though numerical
 447 solutions can always help determine stability (see Section 7.1)). However, we have good
 448 reason to believe that our governing equations are simply not sufficient, given the com-
 449 plex rheology and natural heterogeneity of soliflucting soil. We explore this in the fol-
 450 lowing sections.

451 6 Stability analysis for exponentially increasing viscosity with depth

452 The fluid formulation presented thus far is highly simplistic and therefore is not
 453 able to produce complex vertical velocity profiles observed in the field and lab (Fig. 2).
 454 Here we add an element of complexity and allow effective viscosity to increase with depth
 455 into the soil column, as proposed in (R. C. Glade et al., 2021), interpreted from the ex-
 456 ponentially decreasing velocity and therefore decreasing strain rate with depth (Figure
 457 2) and detailed in section 2.2. We note that this approach is similar to granular formu-
 458 lations like $\mu(I)$ (Jop et al., 2006), though there are two challenges with directly apply-
 459 ing $\mu(I)$ to our system: 1) we lack an understanding of how μ changes with depth and
 460 2) our slow, sub-yield soil motions may not be valid for $\mu(I)$ (Jerolmack & Daniels, 2019).
 461 Therefore, for simplicity, here we use a very simple fluid formulation with viscosity in-
 462 creasing with depth to explore how rheology may affect pattern formation, acknowledg-
 463 ing that we still lack a comprehensive set of governing equations for our system.

464 Let's assume a simplified formulation for effective viscosity in which viscosity μ ex-
 465 ponentially increases with depth into the soil, beginning with a constant viscosity μ_0 at
 466 the surface:

$$\mu(z) = \mu_0 e^{b(H-z)} \quad (21)$$

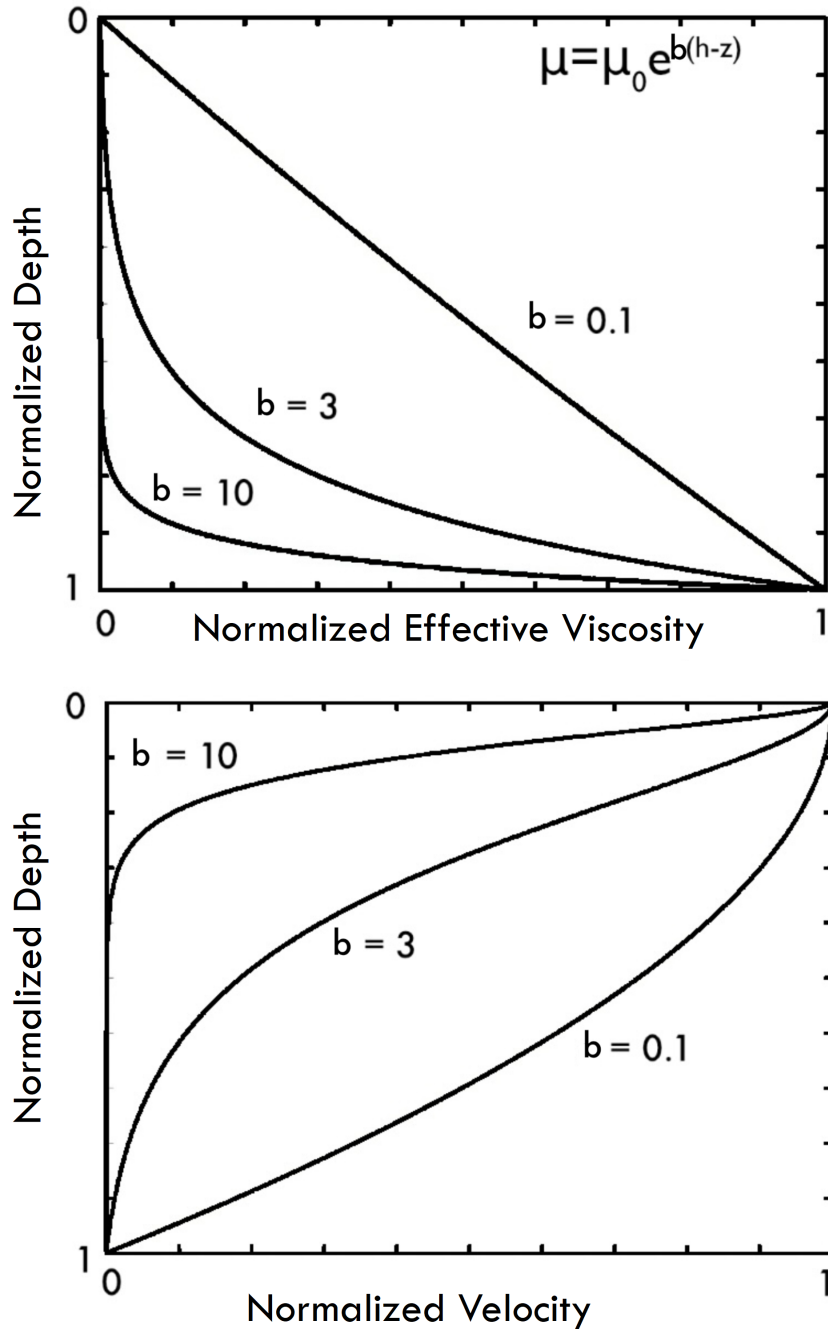


Figure 5. Example normalized vertical profiles of Top) viscosity (Eq. 21) and Bottom) velocity (Eq.22) with depth for different values of scaling factor b .

467

468 where $z=0$ at the base of the soil column and $z=H$ at the surface. Following the same
 469 approach in section 4.1 and using a no slip boundary condition at the base of the soil
 470 column where $z=0$ (Supplementary Materials), we can solve for the x-directed vertical
 471 velocity profile as:

$$u(z) = \frac{\rho g (s - \frac{\partial H}{\partial x})}{\mu_0} \left[\frac{e^{b(z-H)} (b(H-z) + 1)}{b^2} - \frac{e^{-bH} (bH + 1)}{b^2} \right] \quad (22)$$

472

473 Note that for this equation to be valid, $0 < z < h$, and $b > 0$ (i.e., viscosity increases
 474 with depth). With the assumption of Eqn. 22 as a viscosity formulation, this expression
 475 nicely captures the range of behavior seen in field and lab measurements (Fig. 2, 5). For
 476 small b , viscosity increases slowly with depth and the velocity profile resembles that of
 477 a typical fluid. For intermediate b , the velocity profile exhibits an exponential shape at
 478 depth, transitioning to a fluid-like shape at the surface. For high b , the profile is largely
 479 exponential, with the exception of a tiny fluid-like zone at the surface (Fig. 5).

480 We can perform a linear stability analysis to evaluate whether a formulation of this
 481 type could produce an instability leading to the patterns we observe. Following the pro-
 482 cess detailed in section 5.1, with some algebra (Supplementary Materials), we find:

$$\gamma = \left[\frac{2\rho g (e^{-bH_0} - 1)}{\mu_0 b^3} + \frac{2\rho g h_0 e^{-bH_0}}{\mu_0 b^2} + \frac{\rho g H_0^2 e^{-bH_0}}{\mu_0 b} \right] k^2 - \left(\frac{\rho g s H_0^2 e^{-bH_0}}{\mu_0} \right) ik \quad (23)$$

483 It can be shown that if $(\rho, g, \mu_0, b, H_0) > 0$, then the real part of the growth rate
 484 is unconditionally stable (Supplementary Materials). Thus, even though this formula-
 485 tion captures the observed velocity profiles and moves beyond a simple Newtonian fluid,
 486 it is unfortunately not enough to explain the onset of these patterns. We are still miss-
 487 ing some important element of the problem.

488 7 Bump-Dependent Viscosity Inspired by Oobleck Waves

489 So far we have discounted many proposed mechanisms of solifluction instability in-
 490 cluding simple frost creep, buckling instabilities that require compression or multilay-
 491 ers, roll wave instabilities that require inertia, and a depth-dependent viscosity formu-
 492 lation. What are we left with? A pair of recent studies has identified a new type of wave-
 493 like instability that can occur in non-inertial flows. Dubbed "oobleck waves" (Fig. 1G),
 494 this instability is thought to occur due to the unique S-shaped rheological curve of cer-
 495 tain shear-thickening fluids such as oobleck (cornstarch mixed with water) (Texier et al.,
 496 2023; Darbois Texier et al., 2020). The S-shape of the rheological curve refers to a re-
 497 gion where, at high volume fractions (%solid/%liquid), the strain rate bizarrely decreases
 498 as the shear stress increases. This can be thought of as a stress-dependent viscosity, where
 499 viscosity increases as stress increases. In the presence of a bump, higher stress on the
 500 downhill side of the bump increases viscosity there, leading to a growth of the bump (Darbois Tex-
 501 tier et al., 2020). Linear stability analysis shows that this formulation leads to uncondi-
 502 tional instability (Texier et al., 2023) and provides a non-inertial mechanism for wave-
 503 like instabilities at very low Reynolds Number that doesn't rely on external compres-
 504 sion or the presence of multiple layers as in buckling instabilities.

505 Could a similar mechanism be happening with solifluction? Looking at vertical dis-
 506 placement profiles, their exponential shape could point toward a phenomenologically sim-
 507 ilar rheology, because strain rates are highest at the surface where the shear stress is the
 508 lowest and decrease with depth as stress presumably increases (Fig. 2). There is no a

priori expectation for soliflucting soil to actually exhibit shear-thickening rheology akin to oobleck; in fact, soils and other dense geophysical suspensions have been shown to be able to exhibit a wide range of rheology, mostly shear thinning but occasionally shear thickening (Pradeep et al., 2024) or strain hardening (Harris et al., 2003). However, there is ample field evidence that solifluction terraces and lobes experience a slowdown in soil velocity right at the front and edges (e.g., Fig. 2D). There are a variety of plausible mechanisms for this slowdown that do not rely on shear thickening rheology, most of which relate to soil moisture and/or cohesion (see Discussion in (R. C. Glade et al., 2021)). For example, field observations demonstrate enhanced drainage and a lower depth to groundwater table during fall freeze up at terrace fronts and lobe fronts/edges which may decrease both deformation due to frost heave and subsequent downslope motion in the spring (Benedict, 1970). Conversely, once a front is formed, concentration of water during the spring may enhance vegetation growth and stabilize fronts (Eichel et al., 2017; Draebing & Eichel, 2017). Sediment compaction and enhanced cohesion due to capillary bridging may further impede motion at the front. Finally, differences in thermal state at the front could also modify frost heave efficiency (Eichel et al., 2017) (Fig. 10).

7.1 Linear Stability Analysis and Numerical Model

Based on these field observations and the need for a non-inertial source of instability, we use oobleck waves (Texier et al., 2023; Darbois Texier et al., 2020) as inspiration for a possible analogous mechanism that relies not explicitly on soil rheology but topographically dependent properties of the soil (such as soil moisture, thermal state) that may alter effective viscosity near bumps.

For simplicity, our formulation assumes that the effective viscosity depends solely on the downslope gradient (dh/dx) of the free surface; though a dependence on depth is also likely (Section 6), here we isolate the bump-dependent aspect because including both makes the stability analysis prohibitively complex, and because we want to see whether a bump-dependent viscosity alone is enough to produce an instability. We envision that this bump-dependent formulation serves as a rough proxy for spatial variations in physical properties of the soil that control effective soil viscosity or velocity (described above).

We use this simple formulation:

$$\mu(x) = \mu_0 e^{-a \frac{\partial h}{\partial x}} \quad (24)$$

where a is a scaling factor, $\sin \theta$ is the slope of an inclined plane, and x is defined as increasing in the downhill direction. which results in higher viscosity when $\frac{\partial h}{\partial x}$ is negative (i.e., downhill facing bumps) and lower viscosity as $\frac{\partial h}{\partial x}$ increases (thus, uphill faces of bumps have an effectively lower viscosity; e.g., anecdotal field evidence shows surface ponding on lobe treads). This formulation is different from and far simpler than an accurate equation for a shear thickening suspension (e.g., (Wyart & Cates, 2014)). We choose to use this highly simplified equation for μ to capture the essence of the proposed effect—bump dependent viscosity—without appealing to the specifics of rheology, because we simply do not have enough information to be confident in a specific rheology for soliflucting soil (and it is most certainly not strictly oobleckian).

Plugging Eq. 24 into μ in Eq. 3, this results in a velocity profile as follows:

$$u(z) = \frac{\rho g (\sin \theta - \frac{dh}{dx})}{\mu_0 e^{-a \frac{dh}{dx}}} \left(hz - \frac{z^2}{2} \right) \quad (25)$$

According to continuity, the resulting governing equation is:

$$\frac{\partial H}{\partial t} = \frac{\rho g H^2}{3\mu_0} e^{a \frac{\partial H}{\partial x}} \left((1 - a \sin \theta) H \frac{\partial^2 H}{\partial x^2} + \frac{\partial H}{\partial x} \left(a H \frac{\partial^2 H}{\partial x^2} - 3 \sin \theta \right) + 3 \left(\frac{\partial H}{\partial x} \right)^2 \right) \quad (26)$$

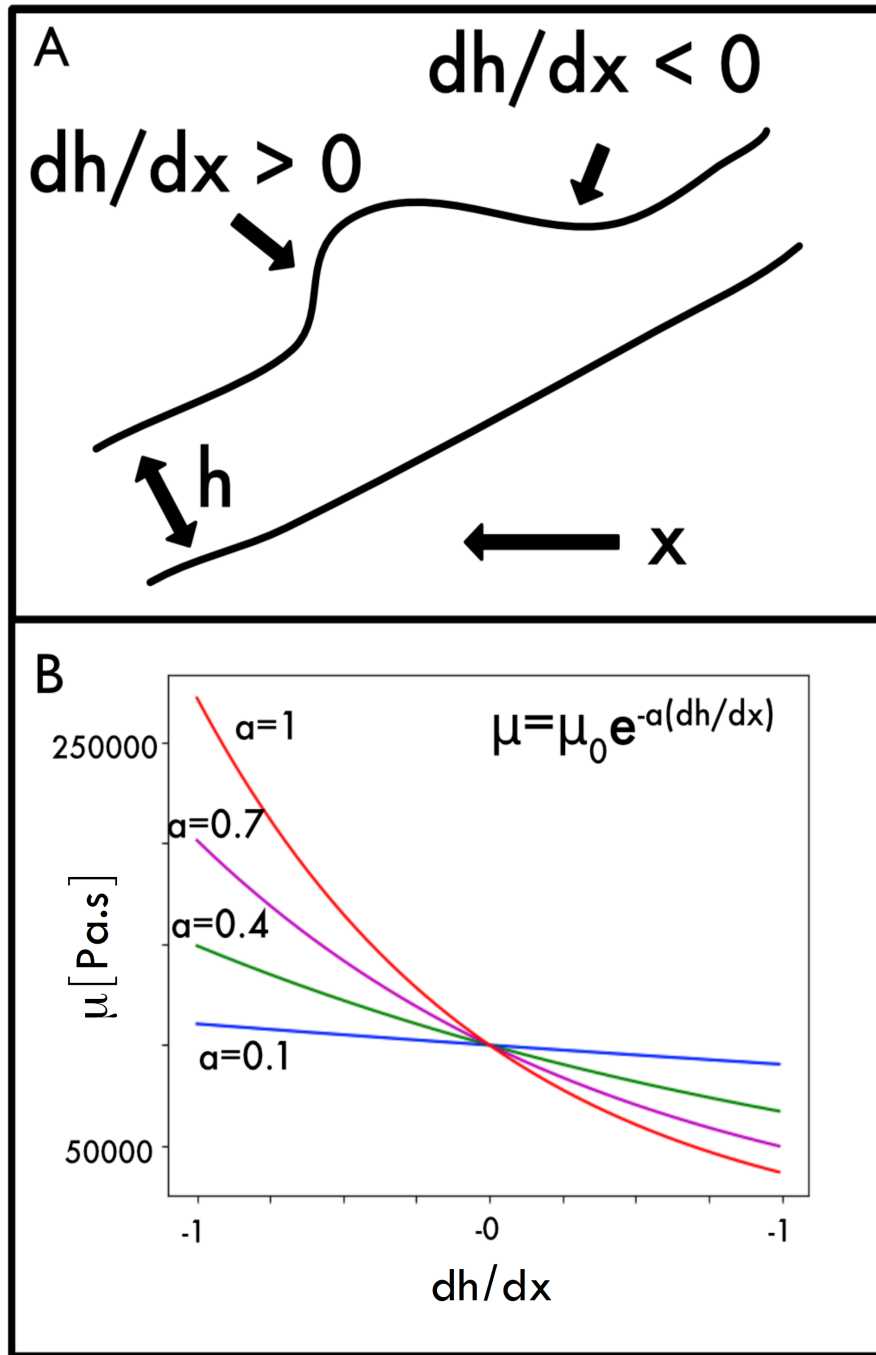


Figure 6. Conceptual figure illustrating bump-dependent viscosity formulation.

(A) Conceptual sketch illustrating positive and negative dh/dx across a topographic bump. Note that x is defined to be positive toward the left in this figure so that it visually corresponds with the plot in part B. h illustrates soil thickness at a given x coordinate (B) corresponding viscosity μ for different values of scaling factor α , illustrating higher viscosity at negative dh/dx values (the downhill side of the bump) and lower viscosity at positive dh/dx values (the uphill side of the bump). In this example, $\mu_0 = 10^5 Pa \cdot s$.

551 Even before conducting our stability analysis, we can see clues about the stability of Eqn.
 552 26 by looking at the equation. A diffusion equation is stable if the diffusivity $D > 0$
 553 and unstable if $D < 0$. Looking at the diffusive term $((1 - a \sin \theta) H \frac{\partial^2 H}{\partial x^2})$, we can see
 554 that the term is only stable when $1 - a \sin \theta$ is positive, or when $a \sin \theta < 1$. Further,
 555 the other term with $\frac{\partial^2 H}{\partial x^2}$ include a $\frac{\partial H}{\partial x}$ in front, meaning this diffusive term is only posi-
 556 tive when $\frac{\partial H}{\partial x} > 0$. It is interesting to note that the $\frac{\partial^2 H}{\partial x^2}$ term is part of the famous
 557 KPZ equation used to describe surface growth and roughening processes (Hairer, 2013).

558 Conducting a linear stability analysis (Supplementary Materials), we find:

$$\gamma = \frac{-\rho g h_0^3 (1 - a \sin \theta)}{3\mu_0} k^2 + (\rho g h_0^2 3 \sin \theta) i k \quad (27)$$

559 This result is (finally) more interesting than the previous analyses we showed! It
 560 has conditional stability; it is stable when $a \sin \theta < 1$, and unstable when $a \sin \theta > 1$.
 561 Unfortunately, however, the form of the resulting growth rate does not give a preferred
 562 wavelength- the growth rate when unstable increases monotonically. This may be due
 563 to finite amplitude effects, in which the nonlinear terms (which we ignored in our linear
 564 stability analysis) are needed to dampen small wavelengths. A key point to note is
 565 that linear stability analysis only predicts the onset of pattern formation, and in the case
 566 of soliflucting soil, would only apply when the soil is actually moving—not during winter
 567 when the soil is considered to be frozen and stationary.

568 7.2 Numerical Exploration

569 To explore this, we run a numerical model of the system in Matlab to explore sta-
 570 bility and wavelength selection when all nonlinear terms are included (solving the con-
 571 tinuity equation through time using Eq. 25 for the vertical velocity profile) (R. Glade,
 572 2026). The model domain is 100m long and consists of a hillslope with a set initial soil
 573 thickness h with a slope of 0.5, soil density = 1500 kg/m³, and initial viscosity of $\mu_0 =$
 574 10^{12} Pa · s. We use a simple euler forward numerical scheme with a spatial step of 1 m.
 575 The model is initialized with a uniform soil thickness (ranging from 1-2 m) with random
 576 perturbations of soil thickness in each cell ranging from 0-.01 m and a timestep $dt = 1/5000$
 577 years to ensure numerical stability. See (R. Glade, 2026) for model code. All models pre-
 578 sented used the same random seed for initial perturbations.

579 We find that, as expected from our analysis, the system is stable for low values of
 580 $a \sin \theta$ and becomes unstable for values of $a \sin \theta > 1$. In contrast to our linear stabil-
 581 ity analysis, however, we observe a soil thickness dependence in the stability criterion
 582 such that increasing initial soil thickness requires lower values of $a \sin \theta$ to become un-
 583 stable; for example, when initial soil thickness is 1m, the system becomes unstable only
 584 when $a \sin \theta > 2$. When initial soil thickness is 2 m, we observe instability around $a \sin \theta >$
 585 1.5. The dependence of stability on soil thickness and the slight deviation from our pre-
 586 dicted critical value of 1 must stem from nonlinear terms that were removed in our linear
 587 stability analysis, of which there are many (Supplementary Materials). The value of
 588 μ_0 does not seem to have a substantial effect on pattern formation beyond setting the
 589 timescale for the development of the patterns; we find that $\mu_0 = 10^{12}$ Pa · s produces
 590 the most reasonable average soil velocities (~ 10 s of cm/s year) and develops meter-scale
 591 terraces within ~ 10 -100 continuous years of deformation, depending on initial soil depth
 592 and choice of parameter a (Figure 7). This is on the shorter side of field measurements
 593 showing solifluction lobe development over timescales ranging from decades to millenia
 594 (Matthews et al., 1986). While time evolution in the model may seem short, this can-
 595 not be directly compared to timescales in the field where soil is frozen stiff for half or
 596 more of the year, and most motion likely takes place within a short span of days or weeks
 597 during spring thaw.

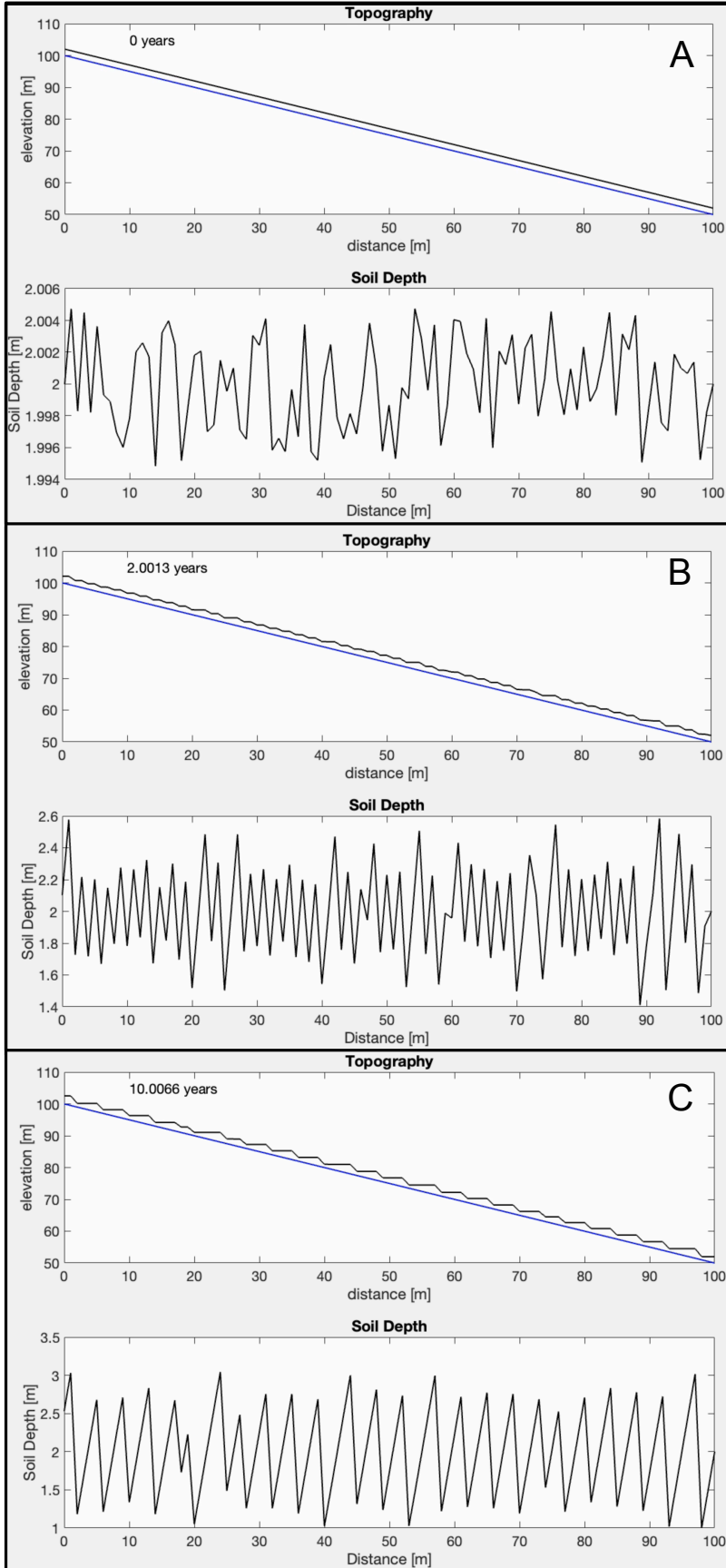


Figure 7. 1D numerical model of terrace formation using the viscosity formulation in Eqn. 25 with $\mu_0 = 10^{12} \text{ Pa} \cdot \text{s}$ shows organized waves developing through time.

598 Similar to the results seen for oobleck waves (Texier et al., 2023), our linear sta-
 599 bility analysis predicted a monotonic increase in growth rate with wavenumber—that
 600 is, no preferred wavelength for instabilities. However, our numerical solution demonstrates
 601 more interesting behavior. Overall, we observe that the initial random perturbation in
 602 soil thickness rapidly self organizes into small, grid-scale waves that continuously coarsen
 603 through time (Figs. 7, 8) (Supplementary Movies). This coarsening behavior indicates
 604 that the nonlinear terms in our governing equation are indeed important, and dominate
 605 over the expected behavior from linear stability analysis (e.g., (Politi & Misbah, 2006)).
 606 Fig. 8 illustrates the change in mean wavelength through time for model runs with three
 607 different initial thicknesses (1-2m) and 3 different values of scaling parameter ($a = 4$ –
 608 6). Mean wavelength was simply calculated as the mean distance between peaks in soil
 609 thickness. Standard deviations are not shown for visual clarity of the plot, but remain
 610 similar between runs on the order of 1 m. Results show that mean wavelength increases
 611 through time for all cases, with a coarsening rate that increases with initial soil thick-
 612 ness. Periods of constant wavelength occur as the bumps grow behind a stalled front,
 613 occasionally reaching a point where they can suddenly move downhill and alter the wave-
 614 length (Movie S1). However, mean wavelength decreases with increasing scaling param-
 615 eter a —that is, the stronger the effect of bump-dependent viscosity, the smaller the re-
 616 sulting wavelength (similar to the fact that contact instability finger wavelength decreases
 617 as surface tension increases (Huppert, 1982)). This makes sense from a conservation of
 618 mass standpoint—if a stronger viscosity effect limits the height at which bumps can con-
 619 tinue to move, there can be a larger number of bumps (and therefore shorter wavelength).
 620 For a lower viscosity effect, bumps can continue to grow and coalesce into larger wave-
 621 lengths. Thus, it is possible that a given terrace wavelength in the field suggests some-
 622 thing about the strength of the effective viscosity effect.

623 Coarsening results in strikingly self-organized waves in all runs. Figure 8 suggests
 624 that maximum wavelengths tend to increase with increasing initial soil thickness. Wave-
 625 length coarsening in the model slows down dramatically over time, likely due to 1) lim-
 626 ited soil thickness available to transport and 2) a drastic increase in effective viscosity
 627 for tall waves such that the soil effectively becomes a solid. This slowdown can also be
 628 seen in videos of oobleck waves (Darbois Texier et al., 2020). In reality, it is likely that
 629 at a certain point the material ceases to behave like a fluid and obeys solid-like behav-
 630 ior, which may allow the front to eventually collapse and rebuild (Section 8; Fig. 10).
 631 It is important to note that the wavelengths produced in our toy model are very likely
 632 dependent on the scale of the initial perturbation, which is set by the grid size. Simi-
 633 larly, in the field, there is likely a minimum size of perturbation required to initiate bump-
 634 dependent soil deformation rates. Modeled terrace height increases through time along
 635 with wavelength, reaching heights on the order of the initial soil thickness (Figure S2).
 636 This agrees with field observations that solifluction lobe and terrace height generally in-
 637 dicate the maximum depth of movement due to frost heave (Matsuoka, 2001). The slow-
 638 down in coarsening through time results in wavelengths on the lower end of the range
 639 of wavelength seen in the field (Figure 10). We did run one model for 10 hours at a lower
 640 viscosity of $\mu_0 = 10^{10}$ Pa · s to enable more efficient terrace formation and observed a
 641 wavelength of ~ 20 m (Figure S3).

642 Our numerical results show that the proposed simple bump-dependent viscosity for-
 643 mulation is capable of producing highly organized waves that strongly resemble solifluc-
 644 tion terraces, importantly without appealing to inertia or multilayer flow. We avoid fur-
 645 ther formal analysis of this numerical model because we have no evidence that the pre-
 646 cise governing equation (which as a reminder, we made up entirely) is valid for our sys-
 647 tem. Rather, this demonstration is to show that a formulation of this general type, with
 648 bump-dependent properties, may be enough to explain the formation of solifluction ter-
 649 races. If we assume that our results are at all illustrative of what could happen in a so-
 650 lifluction system, one could imagine that the wavelengths observed in the field reflect a
 651 complex combination of soil thickness, frost-heave perturbation magnitude, strength of

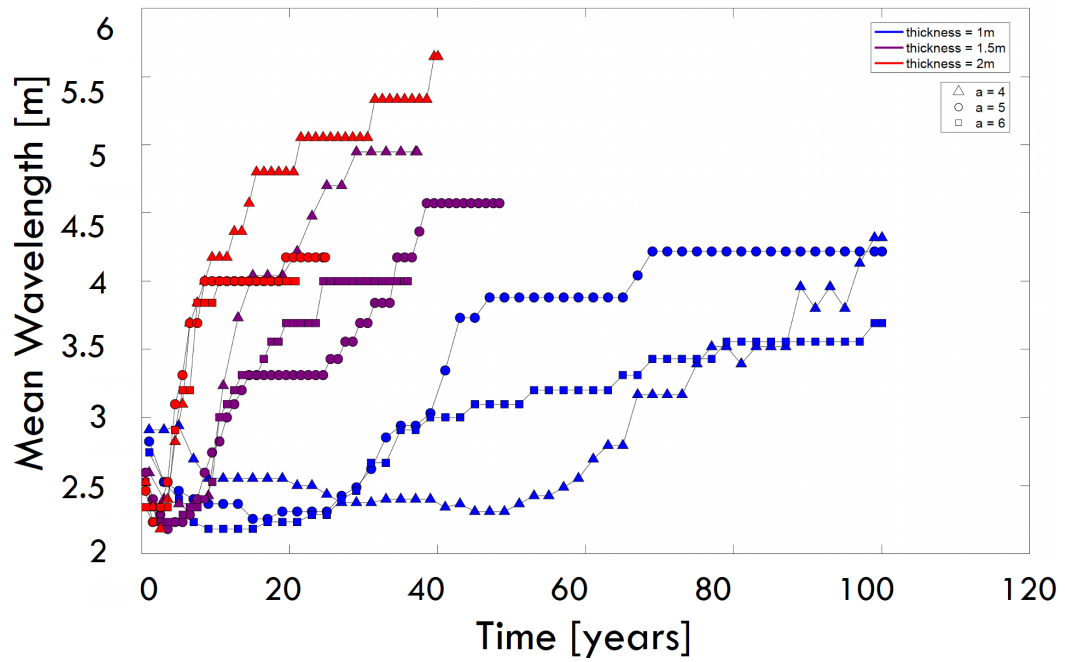


Figure 8. Evolution of mean wavelength through time for 1D model runs with different thickness (colors) and values of scaling parameter a (symbols).

bump-dependent velocity effect, and time since initiation. Perhaps this explains why observations of solifluction wavelengths are so messy (Fig. 4; (R. C. Glade et al., 2021)).

To explore potential 2D effects, we modified our 1D model of flow down an inclined plane to allow flow in the y (cross-slope) direction, using periodic boundary conditions in both the x and y direction with an initial soil thickness of 1.5m and a timestep of 1/20,000 years. To speed up the run time of the model, we use a lower viscosity of $\mu_0 = 10^{10}$ Pa · s. When we use a bump-dependent viscosity in only the x (downhill) direction, with constant viscosity in the y direction, we observe the coalescence of nascent terraces into perfectly straight features that span the width of the domain (Fig. 9A). We also explore the case of bump dependent viscosity in the y direction using the equation:

$$\mu(x) = \mu_0 e^{-a \left| \frac{\partial h}{\partial y} \right|} \quad (28)$$

This differs from the downhill viscosity formulation (Eqn. 24) in that bump dependent viscosity only depends on $|dh/dy|$, with no difference depending on the direction. With bump dependent viscosity in both the x and y direction, we observe the spontaneous formation of lobe-like features at terrace fronts (Fig. 9B). However, cross-slope lobes are not highly organized in our model (i.e., we do not observe a characteristic wavelength). This may be due to the highly simplified 2D model in which soil can only move in 2 directions; perhaps a more advanced model allowing for D8 flow routing would produce more realistic lobes (Movie S3). Of course, a more likely explanation is that our highly simplified model is not capturing the physics of real landscapes, and more complexity would be needed to fully reproduce the observed patterns. Regardless, the 2D model suggests that our bump dependent viscosity formulation has the potential to explain the development both downslope and cross-slope solifluction patterns—an enticing idea! Further, soil conditions and topography at different field sites may favor bump-dependent viscosity only in the downslope direction (resulting in smooth terraces, see Fig. 1A and Fig. 10) or in both the downslope and cross-slope directions (Fig. 1B).

7.3 What Sets Maximum Terrace and Lobe Height?

Our linear stability analysis numerical results show that terrace wavelength coarsening and increase in height may plausibly continue forever, albeit at a slower and slower rate through time as effective viscosity at the front becomes exceedingly high. However, we posit that at a certain height this behavior becomes unrealistic and the material begins to act much more like a solid than a fluid, with a maximum shear strength set by competition between cohesion, internal friction, and shear stress as viewed in classical soil mechanics. Indeed, recent remote observations indicate that soil instabilities may continue to grow until reaching a critical size, at which point failure mechanisms set in to arrest further growth. According to classic mohr-coulomb stability, the maximum height H of a vertical column of soil should scale inversely with gravity (Abramian et al., 2020). Comparison of solifluction lobe height between Earth and Mars showed that lobes on Mars are approximately 2.6 times taller than those on Earth, the precise value expected if lobe height is set by the cohesive strength of the material under different gravitational conditions (Sleiman et al., 2024). This suggests that, in natural systems, a collapse triggered by reaching the soil’s cohesive limit might be the mechanism that ultimately controls the amplitude of the instability. Indeed, many field studies provide evidence of collapse and subsequent advance of solifluction lobe fronts (Kinnard & Lewkowitz, 2006; Williams, 1957; Ridefelt et al., 2009; Ridefelt & Boelhouwers, 2006; Benedict, 1976). (Kinnard & Lewkowitz, 2006) used radiocarbon dating to find that solifluction lobes build up behind a relatively stagnant front, then collapse, then rebuild again in a cycle of \sim hundreds of years. Our work supports this conceptual model of solifluction lobe and terrace advance.

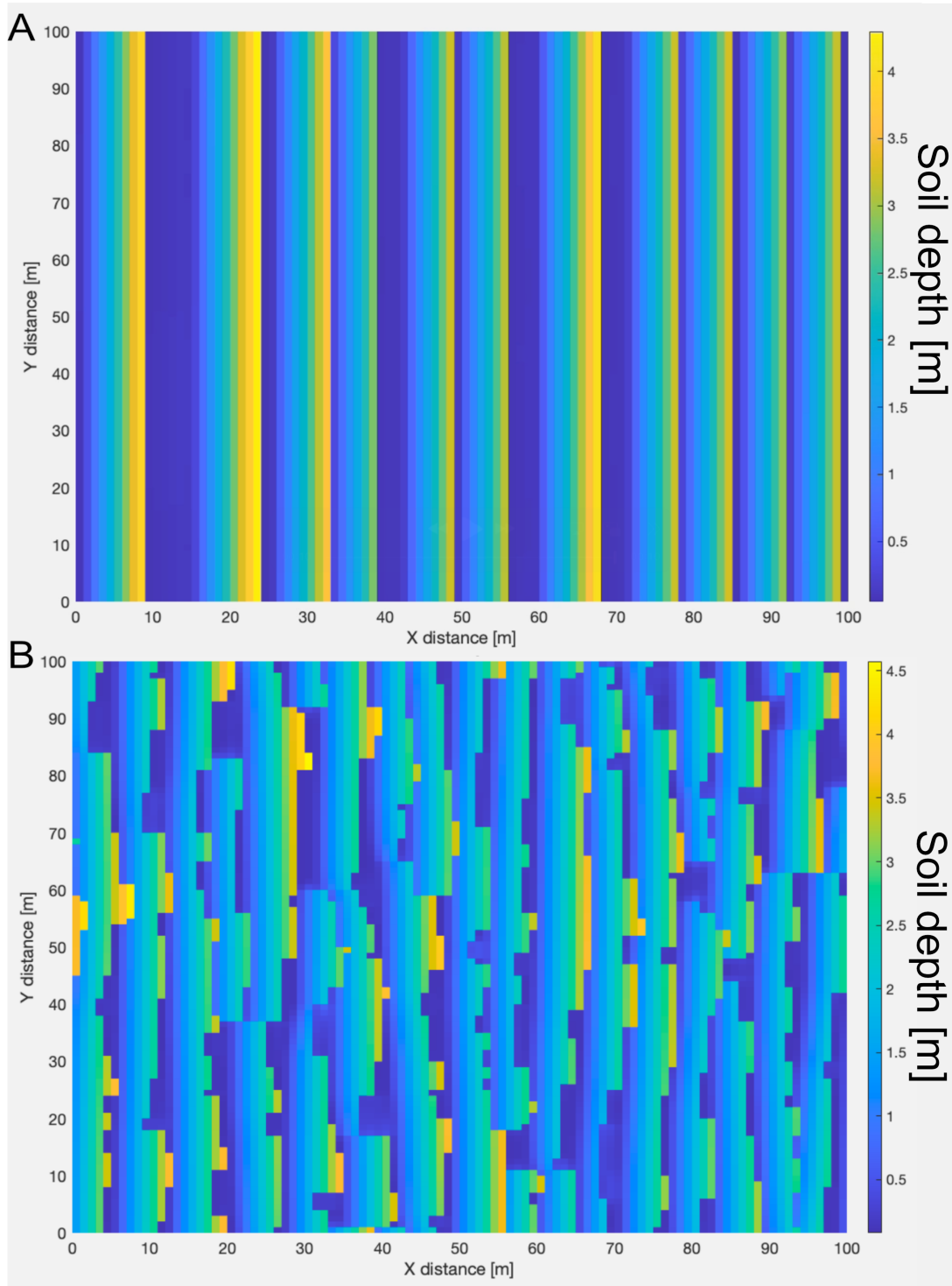


Figure 9. 2D model of terrace formation using a bump-dependent viscosity formulation. Flow is left to right. Initial soil depth is 1.5m and initial viscosity $\mu_0 = 10^{10}$ Pa \cdot s. Colors indicate soil depth (meters). A) Bump dependent viscosity only in downhill x direction; constant viscosity in y direction. B) Bump dependent viscosity with the exponential viscosity parameter $a = 5$ in both the x (downhill) and y (cross slope) direction.

699

8 Conceptual model for solifluction pattern formation

700

701

702

703

704

705

706

707

708

709

710

711

712

Our work has shown many mechanisms (simple frost creep, buckling instabilities, roll waves) that *cannot* explain the onset of solifluction instabilities. While oobleck waves represent a potential analogous non-inertial system, we do not suggest directly comparing these systems because solifluction likely does not behave as a simple shear-thickening fluid; further, if rheology alone were the dominant factor in producing patterns, we may expect to see similar patterns in temperate landscapes (which to our knowledge have not been found). However, we suggest that there is a phenomenological similarity between the two in which a variety of conditions may cause slower soil velocities (and thus an effectively higher viscosity, if using a fluid framework) at the front of bumps, leading to the instability. As discussed above, many plausible natural mechanisms exist for this including spatial and temporal trends in soil moisture, vegetation, and granular compaction (Benedict, 1970; Draebing & Eichel, 2017; Eichel et al., 2017, 2020; Kinnard & Lewkowicz, 2005, 2006).

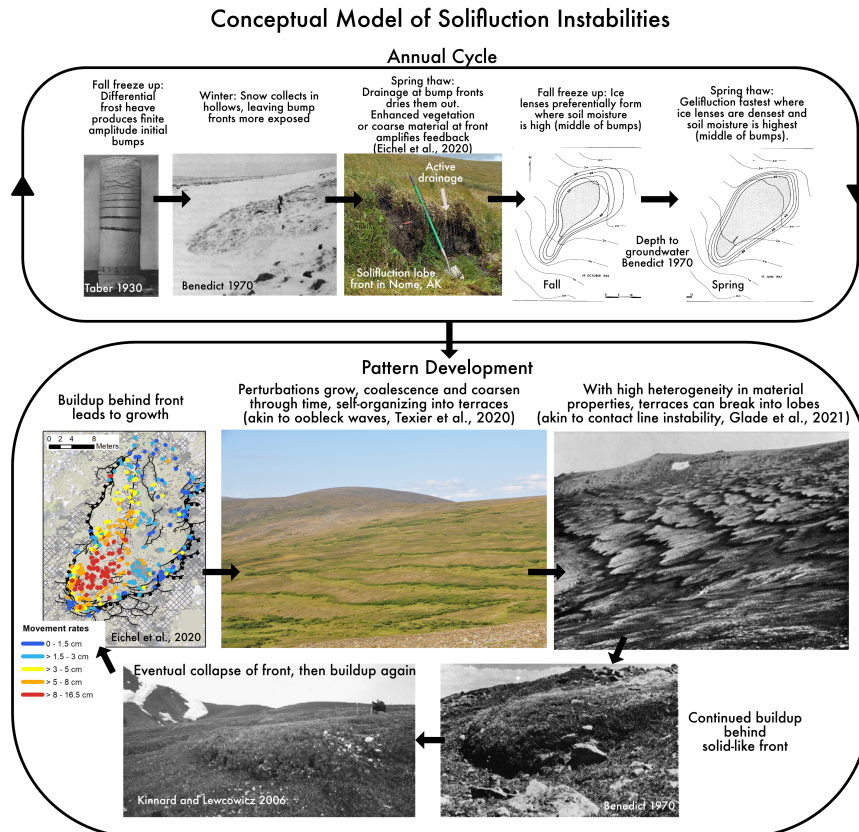


Figure 10. Conceptual model of solifluction instabilities. Top: Annual cycle of frost heave and soil moisture conditions leading to soil buildup behind bumps. Bottom: Buildup behind bumps leads to growth of patterns. Collapse of solid-like fronts allows motion downhill. Note: We use photographs of solifluction lobes in this figure because they are most abundant in the literature; however, illustrations represent roughness elements that ultimately lead to pattern formation.

713

714

715

After evaluating many different possible mechanisms, we propose the three following minimum necessary and sufficient ingredients for the initiation of solifluction-like patterns:

- 716 1) Initial topographic bumps large enough to experience spatial heterogeneity in soil prop-
 717 erties
- 718 2) Rheology or other mechanism (non-inertial) that causes slower soil velocity and there-
 719 fore buildup at the fronts of these bumps
- 720 3) Fronts collapse or roll over once they become too tall, such that they move downhill

721 We propose that these three ingredients are enough to form not only downslope-
 722 oriented solifluction terraces, but likely subsequent solifluction lobes that form at ter-
 723 race fronts (Fig. 9) (R. C. Glade et al., 2021)) (however, to be clear, isolated solifluc-
 724 tion lobes can form not at terrace fronts, likely concentrated in flow paths (van Etten
 725 et al., 2025)). The simplicity and generalized nature of the three ingredients begs the
 726 question of why we only see solifluction patterns in cold places. None of the necessary
 727 and sufficient ingredients above exclusively require ice or frost heave at first glance. How-
 728 ever, we propose that it is only in cold (if not permafrost) landscapes that these key in-
 729 ingredients can be satisfied due to the unique annual processes that occur there on a reg-
 730 ular basis. For the first ingredient, differential frost heave is a highly efficient creator of
 731 significant surface roughness, generating bumps up to a foot in height (Taber, 1930). While
 732 animals, tree throw, and other mechanisms generate roughness in temperate landscapes,
 733 frost heave is one of the only mechanisms that produces substantial roughness reliably
 734 every single year across the entire landscape. For the second ingredient, substantial dif-
 735 ferences in soil velocity are needed across a topographic bump. While there are many
 736 different mechanisms that could accomplish this (see above), by far the most likely would
 737 be due to differences in soil moisture across a bump and soil velocity that is closely con-
 738 nected to soil moisture. Frost creep and gelifluction are highly efficient, soil moisture-
 739 dependent processes that can only be found in cold places. While supersaturated soil on
 740 slopes can occur in temperate regions, this is generally due to rare large storms. In per-
 741 mafrost landscapes the presence of a relatively impermeable permafrost layer decreases
 742 the volume of soil that can accept water, and the soil reliably becomes saturated every
 743 year due to snowmelt, with areas of high moisture content experiencing both higher frost
 744 heave in the winter and stronger gelifluction during spring thaw (Benedict, 1970). It is
 745 also worth considering the idea that variations in subsurface characteristics, e.g. permafrost
 746 and groundwater depth, could lead to instability even in the presence of a flat surface
 747 topography. The third ingredient requires only that the soil has a maximum strength
 748 until it collapses, which should not require cold region dynamics. Note that there is an
 749 abundance of relict solifluction features from the Pleistocene across the eastern US that
 750 formed during colder climates but are no longer active, strengthening the idea that so-
 751 lifluction patterns are indeed unique to cold regions (Merritts & Rahnis, 2022).

752 We have summarized our detailed conceptual model in Fig. 10. At the top of the
 753 figure, we illustrate the conditions that may lead to the first two ingredients: sufficient
 754 initial roughness and buildup behind bumps. After initial roughness is produced by frost
 755 heave in a landscape, we hypothesize that soil moisture conditions are the most impor-
 756 tant element for the second ingredient—buildup behind bumps. Snowfall during the win-
 757 ter tends to concentrate in hollows between bumps and areas of low slope (i.e., the up-
 758 hill side of bumps), leaving the front of bumps more exposed. In the spring, this focuses
 759 thawed water flow into hollows, again leaving bumps drier. During fall freeze up, ice lenses
 760 preferentially form where soil moisture is high, which tends to be on the uphill side or
 761 middle of bumps but not the front (we acknowledge that this effect may potentially be
 762 captured in the diffusive frost creep formulation if the frost heave frequency is depen-
 763 dent on topography (Eqn. 1) (R. S. Anderson & Anderson, 2010)). During spring thaw,
 764 gelifluction will be most efficient where frost heave was highest, leading to higher soil ve-
 765 locities behind the front of bumps. This cycle repeats every year, leading to growth of
 766 bumps and the possible development of solifluction patterns. When the bumps grow too
 767 tall, depending on their materials properties (cohesion, internal friction angle, grain size),
 768 slope and gravity, they collapse and build up again (Fig. 10 bottom). We propose that

769 the reason these patterns are only seen in cold places is that frost heave and gelifluction,
 770 in the presence of large quantities of snow, result in a hillslope system that is highly de-
 771 pendent on soil moisture and flow properties and which experiences strong spatial vari-
 772 ations in these properties every year. In other landscapes, it is plausible that solifluction-
 773 like patterns could form, but these are more likely to be one-off features such as earth
 774 flows or small features after a particularly strong rainstorm. Additionally, the prevalence
 775 of diffusive-like disturbances in temperate landscapes (tree throw, gophers, ants, etc.)
 776 may destroy any features that begin to form.

777 We would be remiss to neglect the likely importance of vegetation and grain size
 778 segregation, which characterize turf-banked and stone-banked lobes, respectively (Benedict,
 779 1970; Ballantyne, 2025). Preferential vegetation growth at the front of terraces and lobes
 780 due to enhanced moisture there during the growing season likely enhances the slowdown
 781 at soil fronts (Eichel et al., 2017; Draebing & Eichel, 2017). Further, feedbacks among
 782 soil temperature, deformation rates, and vegetation heterogeneity may lead to complex
 783 landscape response to a warming climate (Farley et al., 2026). Likewise, granular seg-
 784 regation leads to upfreezing of large stones (S. P. Anderson, 1988) akin to the brazil nut
 785 effect seen in common granular materials (Ottino & Khakhar, 2000) that can lead to gran-
 786 ular fingering instabilities in mixed grain size (Pouliquen et al., 1997). However, we ar-
 787 gue that a spatial trend in soil moisture is the fundamental ingredient needed to form
 788 solifluction patterns given that not all terraces and lobes are stone-banked, and patterns
 789 are able to exist on Mars without vegetation (but without current moisture, instead per-
 790 haps experiencing frost heave due to freezing and sublimation (Sleiman et al., 2024)).
 791 Further experimental and theoretical work would be needed to fully rule out vegetation
 792 and granular segregation as necessary ingredients for solifluction pattern formation. It
 793 is likely that a combination of soil moisture, vegetation, and grain size effects leads to
 794 the characteristic slowdown at soil fronts that we argue is necessary for solifluction pat-
 795 tern formation.

796 A key difficulty in validating our conceptual model is the lack of field sites with clear
 797 proto-solifluction patterns. While previous studies have shown that lobes tens of meters
 798 in wavelength can form in 100 years (Eichel et al., 2017; Draebing & Eichel, 2017), oth-
 799 ers find longer timescales of hundreds to thousands of years (Kinnard & Lewkowicz, 2005;
 800 Matthews et al., 1986). This makes real time observation of solifluction pattern initia-
 801 tion and development impossible with current technology. With high resolution satel-
 802 lite imagery it may be possible to observe initiation of patterns, but if so we would only
 803 have limited data currently of high enough resolution. The lack of proto-patterns is why
 804 we only show images of solifluction lobes for demonstration in Fig. 10; however, note that
 805 these are illustrative and we believe the initial roughness would consist of smaller less-
 806 organized bumps.

807 Still, targeted field measurements could test some of our findings. More studies like
 808 (Eichel et al., 2020) could collect high resolution data on soil velocities and differences
 809 in material properties such as soil moisture, cohesion, and grain size within a solifluc-
 810 tion terrace. Cores could be collected for geotechnical testing of rheological properties
 811 within solifluction terraces and lobes. Physical experiments, though challenging, could
 812 also speed up seasonal cycles and attempt to create solifluction patterns in the lab- some-
 813 thing that’s never been done before (Harris et al., 2008).

814 9 Conclusions

815 In this paper, we have used a combination of theory, numerical modeling, remote
 816 sensing, and literature review to explore many different plausible mechanisms for the ini-
 817 tiation of solifluction terraces. We conclude that despite striking visual similarities, so-
 818 lifluction terraces are not examples of buckling instabilities or roll waves. They also can-
 819 not be explained by classic diffusive-like hillslope formulations. We find that the clos-

est analogous pattern may be oobleck waves, which form due to unique non-newtonian rheology that leads to an increase in effective viscosity on the downhill side of topographic bumps. We argue that soliflucting soil may experience a phenomenologically similar instability in which spatial differences in soil moisture lead to differences in soil velocity, with buildup of soil behind the fronts of topographic bumps that leads to spatial organization of patterns. Based on prior work, we believe this mechanism can explain not only the initiation of solifluction terraces, but also of subsequent solifluction lobes that form at their fronts akin to a contact line instability (R. C. Glade et al., 2021). We hope our work demonstrates the vast potential of comparing geomorphic systems with those found in disparate fields such as fluid and solid mechanics and soft matter physics (Jerolmack & Daniels, 2019); however, we also hope the reader has gained an appreciation for the non-uniqueness of patterns and the many caveats that should be taken into consideration when comparing idealized physics problems with messy natural systems. It is both deeply humbling and inspiring that such a seemingly simple, slow-moving, soil-covered hill can be so enigmatic and rich in behavior.

Open Research Section

All data and code used in this study can be found at (R. Glade, 2026) with the exception of the Norway topographic data from (Fratkin et al., 2021).

Conflict of Interest disclosure

The authors declare there are no conflicts of interest for this manuscript.

Acknowledgments

We would like to acknowledge Bob Anderson and Joel Rowland for introducing us to the beautiful problem of solifluction; David Furbish for a great many insightful conversations about stability analysis and pattern formation; Eric Weeks for a thoughtful read through of the draft; and the attendees of the 2026 KITP Soft Earth Geophysics program for enlightening conversations and feedback.

References

- Abramian, A., Staron, L., & Lagr e, P.-Y. (2020). The slumping of a cohesive granular column: Continuum and discrete modeling. *Journal of Rheology*, *64*(5), 1227–1235.
- Anderson, R. S., & Anderson, S. P. (2010). *Geomorphology: the mechanics and chemistry of landscapes*. Cambridge University Press.
- Anderson, S. P. (1988). The upfreezing process: experiments with a single clast. *Geological Society of America Bulletin*, *100*(4), 609–621.
- Andersson, J. G. (1906). Solifluction, a component of subaerial denudation. *The Journal of Geology*, *14*(2), 91–112.
- Ballantyne, C. K. (2013). A 35-year record of solifluction in a maritime periglacial environment. *Permafrost and Periglacial Processes*, *24*(1), 56–66.
- Ballantyne, C. K. (2025). Periglacial vegetation-banked terraces: A global survey. *Permafrost and Periglacial Processes*, *36*(4), 715–738.
- Balmforth, N., & Liu, J. (2004). Roll waves in mud. *Journal of Fluid Mechanics*, *519*, 33–54.
- Balmforth, N. J., Craster, R., & Slim, A. C. (2008). On the buckling of elastic plates. *The Quarterly Journal of Mechanics & Applied Mathematics*, *61*(2), 267–289.
- Benedict, J. B. (1970). Downslope soil movement in a colorado alpine region: rates, processes, and climatic significance. *Arctic and Alpine Research*, *2*(3),

- 165–226.
- 867 Benedict, J. B. (1976). Frost creep and gelifluction features: a review. *Quaternary*
868 *Research*, 6(1), 55–76.
- 869 Biot, M. A. (1961). Theory of folding of stratified viscoelastic media and its im-
870 plications in tectonics and orogenesis. *Geological Society of America Bulletin*,
871 72(11), 1595–1620.
- 872 Blake, K., & Bejan, A. (1984). Experiments on the buckling of thin fluid layers un-
873 dergoing end-compression.
- 874 Chandrasekhar, S. (2013). *Hydrodynamic and hydromagnetic stability*. Courier Cor-
875 poration.
- 876 Chang, H.-C., et al. (1994). Wave evolution on a falling film. *Annual review of fluid*
877 *mechanics*, 26(1), 103–136.
- 878 Coffey, N. B., MacAyeal, D. R., Copland, L., Mueller, D. R., Sergienko, O. V., Ban-
879 well, A. F., & Lai, C.-Y. (2022). Enigmatic surface rolls of the ellesmere ice
880 shelf. *Journal of Glaciology*, 68(271), 867–878.
- 881 Darbois Texier, B., Lhuissier, H., Forterre, Y., & Metzger, B. (2020). Surface-wave
882 instability without inertia in shear-thickening suspensions. *Communications*
883 *Physics*, 3(1), 232.
- 884 Del Vecchio, J., Lathrop, E., Dann, J. B., Andresen, C. G., Collins, A. D., Fratkin,
885 M. M., ... Rowland, J. C. (2022). Patterns and rates of soil movement
886 and shallow failures across several small watersheds on the seaward peninsula,
887 alaska. *Earth Surface Dynamics Discussions*, 2022, 1–28.
- 888 Depoilly, F., Millet, S., Ben Hadid, H., Dagois-Bohy, S., & Rousset, F. (2024). Uni-
889 fying the roll waves. *PLoS one*, 19(11), e0310805.
- 890 Deshpande, N. S., Furbish, D. J., Arratia, P. E., & Jerolmack, D. J. (2021). The
891 perpetual fragility of creeping hillslopes. *Nature Communications*, 12(1),
892 3909.
- 893 Draebing, D., & Eichel, J. (2017). Spatial controls of turf-banked solifluction lobes
894 and their role for paraglacial adjustment in glacier forelands. *Permafrost and*
895 *Periglacial Processes*, 28(2), 446–459.
- 896 Eichel, J., Draebing, D., Kattenborn, T., Senn, J. A., Klingbeil, L., Wieland, M.,
897 & Heinz, E. (2020). Unmanned aerial vehicle-based mapping of turf-banked
898 solifluction lobe movement and its relation to material, geomorphometric, ther-
899 mal and vegetation properties. *Permafrost and Periglacial Processes*, 31(1),
900 97–109.
- 901 Eichel, J., Draebing, D., Klingbeil, L., Wieland, M., Eling, C., Schmidlein, S., ...
902 Dikau, R. (2017). Solifluction meets vegetation: the role of biogeomorphic
903 feedbacks for turf-banked solifluction lobe development. *Earth Surface Pro-*
904 *cesses and Landforms*, 42(11), 1623–1635.
- 905 Farley, M. S., Thaler, E. A., Fiolleau, S., Dafflon, B., Del Vecchio, J., Wang, C., ...
906 Rowland, J. (2026). Vegetation heterogeneity reflects soil thermal state and
907 surface soil displacement in a thawing permafrost landscape. *Environmental*
908 *Research: Ecology*.
- 909 Fink, J. (1980). Surface folding and viscosity of rhyolite flows. *Geology*, 8(5), 250–
910 254.
- 911 Fiolleau, S., Uhlemann, S., Shirley, I., Wang, C., Wielandt, S., Rowland, J., & Daf-
912 flon, B. (2024). Insights on seasonal solifluction processes in warm permafrost
913 arctic landscape using a dense monitoring approach across adjacent hillslopes.
914 *Environmental Research Letters*, 19(4), 044021.
- 915 Fratkin, M., Glade, R., Nutt, M., Pouragha, M., Seiphoori, A., & Rowland, J.
916 (2021). *Arctic soil patterns analogous to fluid instabilities: Supporting data*.
917 Next-Generation Ecosystem Experiments (NGEE) Arctic, ESS-DIVE reposi-
918 tory. [Dataset] doi:10.5440/1768024.
- 919 French, H. M. (2017). *The periglacial environment*. John Wiley & Sons.
- 920 Furbish, D. J., Roering, J. J., Doane, T. H., Roth, D. L., Williams, S. G., & Abbott,

- 922 A. M. (2021). Rarefied particle motions on hillslopes—part 1: Theory. *Earth*
 923 *Surface Dynamics*, 9(3), 539–576.
- 924 Gastineau, R., Conway, S. J., Johnsson, A., Eichel, J., Mangold, N., Grindrod,
 925 P. M., & Izquierdo, T. (2020). Small-scale lobate hillslope features on mars:
 926 A comparative 3d morphological study with terrestrial solifluction lobes and
 927 zebra stripe lobes. *Icarus*, 342, 113606.
- 928 Glade, R. (2026). *Data for “exploring potential mechanisms for the initiation of so-*
 929 *lifluction patterns”*. Zenodo, v1. [Dataset] doi:10.5281/zenodo.20193053.
- 930 Glade, R. C., Fratkin, M. M., Pouragha, M., Seiphoori, A., & Rowland, J. C. (2021).
 931 Arctic soil patterns analogous to fluid instabilities. *Proceedings of the National*
 932 *Academy of Sciences*, 118(21), e2101255118.
- 933 Griffiths, R. W. (2000). The dynamics of lava flows. *Annual review of fluid mechan-*
 934 *ics*, 32(1), 477–518.
- 935 Guazzelli, É., & Pouliquen, O. (2018). Rheology of dense granular suspensions.
 936 *Journal of Fluid Mechanics*, 852, P1.
- 937 Hairer, M. (2013). Solving the kpz equation. *Annals of mathematics*, 559–664.
- 938 Harkema, M., Nijland, W., de Jong, S., Kattenborn, T., & Eichel, J. (2023). Mon-
 939 itoring solifluction movement in space and time: A semi-automated high-
 940 resolution approach. *Geomorphology*, 433, 108727.
- 941 Harris, C. (1993). The role of climatic and soil properties in periglacial solifluction:
 942 Evidence from laboratory simulation experiments. *Solifluction and Climatic*
 943 *Variations in the Holocene, Special Issue: ESF Project European Paleoclimate*
 944 *and Man*.
- 945 Harris, C. (1996). Physical modelling of periglacial solifluction: Review and future
 946 strategy. *Permafrost and Periglacial Processes*, 7(4), 349–360.
- 947 Harris, C., & Davies, M. C. (2000). Gelifluction: observations from large-scale labo-
 948 ratory simulations. *Arctic, Antarctic, and Alpine Research*, 32(2), 202–207.
- 949 Harris, C., Davies, M. C., & Coutard, J.-P. (1997). Rates and processes of
 950 periglacial solifluction: an experimental approach. *Earth Surface Processes*
 951 *and Landforms: The Journal of the British Geomorphological Group*, 22(9),
 952 849–868.
- 953 Harris, C., Davies, M. C., & Rea, B. R. (2003). Gelifluction: viscous flow or plas-
 954 tic creep? *Earth Surface Processes and Landforms: The Journal of the British*
 955 *Geomorphological Research Group*, 28(12), 1289–1301.
- 956 Harris, C., Kern-Luetschg, M., Murton, J., Font, M., Davies, M., & Smith, F.
 957 (2008). Solifluction processes on permafrost and non-permafrost slopes: results
 958 of a large-scale laboratory simulation. *Permafrost and Periglacial Processes*,
 959 19(4), 359–378.
- 960 Houssais, M., Ortiz, C. P., Durian, D. J., & Jerolmack, D. J. (2016). Rheology of
 961 sediment transported by a laminar flow. *Physical Review E*, 94(6), 062609.
- 962 Huppert, H. E. (1982). Flow and instability of a viscous current down a slope. *Nat-*
 963 *ure*, 300(5891), 427–429.
- 964 Jaesche, P., Veit, H., & Huwe, B. (2003). Snow cover and soil moisture controls
 965 on solifluction in an area of seasonal frost, eastern alps. *Permafrost and*
 966 *Periglacial Processes*, 14(4), 399–410.
- 967 Jerolmack, D. J., & Daniels, K. E. (2019). Viewing earth’s surface as a soft-matter
 968 landscape. *Nature Reviews Physics*, 1(12), 716–730.
- 969 Johnsson, A., Reiss, D., Hauber, E., Zanetti, M., Hiesinger, H., Johansson, L., &
 970 Olvmo, M. (2012). Periglacial mass-wasting landforms on mars suggestive
 971 of transient liquid water in the recent past: Insights from solifluction lobes on
 972 svalbard. *Icarus*, 218(1), 489–505.
- 973 Jop, P., Forterre, Y., & Pouliquen, O. (2006). A constitutive law for dense granular
 974 flows. *Nature*, 441(7094), 727–730.
- 975 Kapitza, P. L. (1949). Wave flow of thin viscous liquid films. iii. experimental study
 976 of wave regime of a flow. *J. Exp. Theor. Phys.*, 19(2), 105–120.

- 977 Kessler, M., & Werner, B. (2003). Self-organization of sorted patterned ground. *Sci-*
 978 *ence*, *299*(5605), 380–383.
- 979 Kinnard, C., & Lewkowicz, A. G. (2005). Movement, moisture and thermal condi-
 980 tions at a turf-banked solifluction lobe, kluane range, yukon territory, canada.
 981 *Permafrost and Periglacial Processes*, *16*(3), 261–275.
- 982 Kinnard, C., & Lewkowicz, A. G. (2006). Frontal advance of turf-banked solifluc-
 983 tion lobes, kluane range, yukon territory, canada. *Geomorphology*, *73*(3-4),
 984 261–276.
- 985 Lachenbruch, A. H. (1962). *Mechanics of thermal contraction cracks and ice-wedge*
 986 *polygons in permafrost* (Vol. 70). Geological Society of America.
- 987 Li, A., Matsuoka, N., Niu, F., Chen, J., Ge, Z., Hu, W., . . . others (2021). Ice
 988 needles weave patterns of stones in freezing landscapes. *Proceedings of the*
 989 *National Academy of Sciences*, *118*(40), e2110670118.
- 990 Loewenherz, D. S., Lawrence, C. J., & Weaver, R. L. (1989). On the development of
 991 transverse ridges on rock glaciers. *Journal of Glaciology*, *35*(121), 383–391.
- 992 Matsuoka, N. (2001). Solifluction rates, processes and landforms: a global review.
 993 *Earth-Science Reviews*, *55*(1-2), 107–134.
- 994 Matsuoka, N. (2010). Solifluction and mudflow on a limestone periglacial slope
 995 in the swiss alps: 14 years of monitoring. *Permafrost and periglacial processes*,
 996 *21*(3), 219–240.
- 997 Matsuoka, N., & Hirakawa, K. (2000). Solifluction resulting from one-sided and two-
 998 sided freezing: field data from svalbard. *Polar geoscience*, *13*, 187–201.
- 999 Matsuoka, N., Ikeda, A., & Date, T. (2005). Morphometric analysis of solifluction
 1000 lobes and rock glaciers in the swiss alps. *Permafrost and Periglacial Processes*,
 1001 *16*(1), 99–113.
- 1002 Matsuoka, N., & Moriwaki, K. (1992). Frost heave and creep in the sør rondane
 1003 mountains, antarctica. *Arctic and Alpine Research*, *24*(4), 271–280.
- 1004 Matthews, J. A., Harris, C., & Ballantyne, C. K. (1986). Studies on a gelifluction
 1005 lobe, jotunheimen, norway: 14c chronology, stratigraphy, sedimentology and
 1006 palaeoenvironment. *Geografiska Annaler: Series A, Physical Geography*, *68*(4),
 1007 345–360.
- 1008 Merritts, D. J., & Rahnis, M. A. (2022). Pleistocene periglacial processes and land-
 1009 forms, mid-atlantic region, eastern united states. *Annual Review of Earth and*
 1010 *Planetary Sciences*, *50*(1), 541–592.
- 1011 Ottino, J. M., & Khakhar, D. V. (2000). Mixing and segregation of granular materi-
 1012 als. *Annual review of fluid mechanics*, *32*(1), 55–91.
- 1013 Pawlik, L., & Šamonil, P. (2018). Soil creep: the driving factors, evidence and
 1014 significance for biogeomorphic and pedogenic domains and systems—a critical
 1015 literature review. *Earth-Science Reviews*, *178*, 257–278.
- 1016 Peppin, S. S., & Style, R. W. (2013). The physics of frost heave and ice-lens growth.
 1017 *Vadose Zone Journal*, *12*(1), 1–12.
- 1018 Politi, P., & Misbah, C. (2006). Nonlinear dynamics in one dimension: A criterion
 1019 for coarsening and its temporal law. *Physical Review E—Statistical, Nonlinear,*
 1020 *and Soft Matter Physics*, *73*(3), 036133.
- 1021 Pouliquen, O., Delour, J., & Savage, S. B. (1997). Fingering in granular flows. *Nature*,
 1022 *386*(6627), 816–817.
- 1023 Pradeep, S., Arratia, P. E., & Jerolmack, D. J. (2024). Origins of complexity in the
 1024 rheology of soft earth suspensions. *Nature communications*, *15*(1), 7432.
- 1025 Price, L. W. (1991). Subsurface movement on solifluction slopes in the ruby range,
 1026 yukon territory, canada—a 20-year study. *Arctic and Alpine Research*, *23*(2),
 1027 200–205.
- 1028 Rempel, A. (2007). Formation of ice lenses and frost heave. *Journal of Geophysical*
 1029 *Research: Earth Surface*, *112*(F2).
- 1030 Ribe, N. M. (2003). Periodic folding of viscous sheets. *Physical Review E*, *68*(3),
 1031 036305.

- 1032 Ribe, N. M. (2004). Coiling of viscous jets. *Proceedings of the Royal Society of Lon-*
 1033 *don. Series A: Mathematical, Physical and Engineering Sciences*, 460(2051),
 1034 3223–3239.
- 1035 Ribe, N. M., Stutzmann, E., Ren, Y., & Van Der Hilst, R. (2007). Buckling instabil-
 1036 ities of subducted lithosphere beneath the transition zone. *Earth and Planetary*
 1037 *Science Letters*, 254(1-2), 173–179.
- 1038 Ridefelt, H., & Boelhouwers, J. (2006). Observations on regional variation in so-
 1039 liffuction landform morphology and environment in the abisko region, northern
 1040 sweden. *Permafrost and Periglacial Processes*, 17(3), 253–266.
- 1041 Ridefelt, H., Boelhouwers, J., & Eiken, T. (2009). Measurement of soliffuction rates
 1042 using multi-temporal aerial photography. *Earth Surface Processes and Land-*
 1043 *forms*, 34(5), 725–737.
- 1044 Rowland, J., Jones, C., Altmann, G., Bryan, R., Crosby, B., Hinzman, L., . . . others
 1045 (2010). Arctic landscapes in transition: responses to thawing permafrost. *Eos,*
 1046 *Transactions American Geophysical Union*, 91(26), 229–230.
- 1047 Skorobogatiy, M., & Mahadevan, L. (2000). Folding of viscous sheets and filaments.
 1048 *Europhysics Letters*, 52(5), 532.
- 1049 Sleiman, J., Conway, S., Johnsson, A., Wray, J., & Glade, R. (2024). Viewing lobate
 1050 patterns on mars and earth as climate modulated fluid-like instabilities.
- 1051 Slim, A. C., Balmforth, N. J., Craster, R., & Miller, J. C. (2009). Surface wrinkling
 1052 of a channelized flow. *Proceedings of the Royal Society A: Mathematical, Physi-*
 1053 *cal and Engineering Sciences*, 465(2101), 123–142.
- 1054 Slim, A. C., Teichman, J., & Mahadevan, L. (2012). Buckling of a thin-layer couette
 1055 flow. *Journal of fluid mechanics*, 694, 5–28.
- 1056 Smith, D. J. (1988). Rates and controls of soil movement on a soliffuction slope in
 1057 the mount rae area, canadian rocky mountains. *Zeitschrift für Geomorphologie*
 1058 *NF*, 71, 25–44.
- 1059 Smith, M. K. (1990). The mechanism for the long-wave instability in thin liquid
 1060 films. *Journal of Fluid Mechanics*, 217, 469–485.
- 1061 Taber, S. (1930). The mechanics of frost heaving. *The Journal of Geology*, 38(4),
 1062 303–317.
- 1063 Texier, B. D., Lhuissier, H., Metzger, B., & Forterre, Y. (2023). Shear-thickening
 1064 suspensions down inclines: from kapitza to oobleck waves. *Journal of Fluid*
 1065 *Mechanics*, 959, A27.
- 1066 Treagus, S. H. (1973). Buckling stability of a viscous single-layer system, oblique to
 1067 the principal compression. *Tectonophysics*, 19(3), 271–289.
- 1068 van Etten, J., Eichel, J., & Draebing, D. (2025). Periglacial puzzles: unravelling en-
 1069 vironmental controls on soliffuction lobes. In *Egu general assembly conference*
 1070 *abstracts* (pp. EGU25–678).
- 1071 Wang, Q., & Zhao, X. (2015). A three-dimensional phase diagram of growth-induced
 1072 surface instabilities. *Scientific reports*, 5(1), 8887.
- 1073 Whitehead, J. A. (1988). Fluid models of geological hotspots. *Annual Review of*
 1074 *Fluid Mechanics*, 20(1), 61–87.
- 1075 Williams, P. (1957). Some investigations into soliffuction features in norway. *The*
 1076 *Geographical Journal*, 123(1), 42–55.
- 1077 Wyart, M., & Cates, M. E. (2014). Discontinuous shear thickening without inertia in
 1078 dense non-brownian suspensions. *Physical review letters*, 112(9), 098302.